https://doi.org/10.5194/amt-2022-245
Preprint. Discussion started: 28 September 2022

Atmospheric Measurement Techniques Discussions

High spatial resolution retrieval of cloud droplet size distribution from polarized observations of the cloudbow

Veronika Pörtge[1], Tobias Kölling[2], Anna Weber[1], Lea Volkmer[1], Claudia Emde[1], Tobias Zinner[1], and Bernhard Mayer[1]

[1]Meteorologisches Institut, Ludwig-Maximilians-Universität München, Munich, Germany
[2]Max Planck Institute for Meteorology, Hamburg, Germany

Correspondence: Veronika Pörtge (veronika.poertge@physik.uni-muenchen.de)

Abstract.

The cloud droplet size distribution is often described by a gamma distribution defined by the effective radius (r_{eff}) and the effective variance (v_{eff}). The effective radius is directly related to the cloud's optical thickness which influences the radiative properties of a cloud. The effective variance affects, among other things, the evolution of precipitation. Both parameters can be retrieved from measurements of the cloudbow. The cloudbow or rainbow is an optical phenomenon, which forms by single scattering of radiation by liquid cloud droplets at the cloud edge. The polarized radiance of the cloudbow crucially depends on the cloud droplet size distribution. r_{eff} and v_{eff} can be retrieved by fitting model simulations (stored in a look-up table) to polarized cloudbow observations.

This study uses measurements from the wide-field polarization-sensitive camera of the LMU spectral imager system specMACS onboard the German research airplane HALO. Together with precise cloud geometry data derived by a stereographic method, a geolocalization of the observed clouds is possible. Observations of the same cloud from consecutive images are combined into one radiance measurement from multiple angles. Two case studies of trade wind cumulus clouds measured during the EUREC^{4}A field campaign are presented and the cloudbow technique is demonstrated. The results are combined into maps of r_{eff} and v_{eff} with a spatial resolution of $100\,\mathrm{m}$ by $100\,\mathrm{m}$ and large coverage (across-track swath width: $8\,\mathrm{km}$). The first case study shows a stratiform cloud deck with distinct patches of large effective radii up to $40\,\mu\mathrm{m}$ and a median effective variance of 0.12. The second case study consists of small cumulus clouds (diameters of approximately $2\,\mathrm{km}$). The retrieved r_{eff} is $6.92\,\mu\mathrm{m}$ and v_{eff} is 0.07 (both median values).

1 Introduction

Clouds have two major implications on Earth's climate system: First, they do not only contribute to the surface energy budget through latent heat release but also directly interact with solar and terrestrial radiation. Second, clouds produce precipitation, which greatly influences our lives, especially in the case of extreme precipitation. Clouds still are the largest uncertainty in predictions of future temperature changes caused by changing greenhouse gas contributions (IPCC, 2021). Although the understanding has improved due to more and better observations as well as new cloud modeling approaches, the influence of clouds remains a large uncertainty in predicting future temperature changes. This is why there is a great interest in extending our knowledge of clouds.

There are several past and planned field campaigns that aim at better understanding clouds and cloud feedback mechanisms (e.g., Arctic Cloud Observations Using Airborne Measurements during Polar Day (ACLOUD) and Physical Feedbacks of Arctic Boundary Layer, Sea Ice, Cloud and Aerosol (PASCAL), both presented in Wendisch et al. (2019), or the Next-Generation Aircraft Remote Sensing for Validation studies (NARVAL), see Stevens et al. (2019)). One such field campaign that put enormous effort into understanding clouds was EUREC^{4}A (ElUcidating the RolE of Cloud-Circulation Coupling in ClimAte). The campaign took place in January and February 2020 and had its base in Barbados (Bony et al., 2017; Stevens et al., 2021). The goal was to intensely measure trade-wind clouds, which are the most frequent cloud type on Earth and therefore crucial for Earth's radiation budget. These clouds and how they react to climate change are a major source of uncertainty in climate sensitivity across different climate models (Bony and Dufresne, 2005). One of the many measurement platforms involved was the German research airplane HALO which was configured as a cloud-observatory similar to the previous NARVAL-II HALO campaign with radar, radiometer, lidar, and different spectral imagers (Stevens et al., 2019; Konow et al., 2021). The subject of this paper, the cloud camera system specMACS (Ewald et al., 2016) was also part of the HALO payload.

While EUREC^{4}A studied clouds at many different scales, here we focus on observations of the microphysical properties of liquid water clouds. Two parameters are of particular importance: The effective droplet size and the width of the cloud droplet size distribution. The effective droplet size determines the radiative effect of clouds on the energy budget: A smaller droplet size (at a constant liquid water content) results in a large part of the incoming solar radiation being reflected at the cloud (Twomey, 1974). The width of the cloud droplet size distribution, e.g., influences the evolution of precipitation (Brenguier and Chaumat, 2001). Often, the effective radius (r_{eff}) is used as a quantitative description of the droplet size, and the width of the size distribution is characterized by the effective variance (v_{eff}) (Hansen, 1971).

Cloud droplet size retrievals are often based on the bi-spectral technique which uses radiance measurements at two different wavelengths (Nakajima and King, 1990). Measurements at a wavelength where scattering dominates such as $0.75\,\mu\mathrm{m}$ are combined with measurements at an absorbing wavelength (e.g., $2.16\,\mu\mathrm{m}$). The radiance in the non-absorbing wavelength is sensitive to the optical thickness of the cloud while the radiance in the absorbing wavelength is sensitive to the effective radius of the cloud. This method simultaneously retrieves effective radius and optical thickness and is widely used for satellite instruments such as the Moderate Resolution Imaging Spectroradiometer (MODIS) (Platnick et al., 2003). The technique is well established, but it has some difficulties which are mainly related to 3-D effects occurring especially in inhomogeneous cumulus cloud fields (Marshak et al., 2006; Zinner et al., 2008; Ewald et al., 2019). Furthermore, retrieving the effective variance of the cloud droplet size distribution is not possible.

In recent years the use of polarized measurements for the retrieval of cloud (and aerosol) optical properties has become more and more popular (e.g., Bréon and Goloub (1998); Alexandrov et al. (2012a); Diner et al. (2013); Remer et al. (2019); McBride et al. (2020)). Polarized measurements have the advantage that multiple scattered contributions are filtered out and single scattering dominates the signal (Hansen, 1971). This greatly reduces 3-D effects which simplifies the analysis. Based on polarized observations of the cloudbow, a new retrieval has emerged: the so-called polarimetric technique. This method determines both the effective radius and effective variance of the cloud droplet size distribution from polarized radiance measurements. The polarized radiance of liquid water clouds is sensitive to the effective radius and the effective variance in two regions: First, in the region of the backscatter glory (scattering angle from 170° to 180°) and second, in the cloudbow or rainbow region (135° to 165°). Both phenomena are described by Mie theory (Mie, 1908; Hansen, 1971). The polarimetric retrieval fits polarized phase functions against the measured polarized radiance (Bréon and Goloub, 1998) and will be discussed in more detail in Section 3.3. In general, unpolarized images also show the glory and the cloudbow and have already been successfully evaluated in terms of the droplet size distribution (e.g., Mayer et al., 2004). But especially for the cloudbow, the contrast in unpolarized observations is usually weak because the signal is dominated by the multiple scattering background. The use of polarized observations significantly enhances the signal.

One important aspect is to determine from which height within the cloud the measured signal originates. Here, the polarimetric retrieval has an advantage over the bi-spectral method: The bi-spectral signals come from a certain, not well defined, distance within the cloud as the photons are scattered multiple times until reaching the sensor (Platnick, 2000). The polarized signal, however, emerges from the cloud top (about 1 optical depth within the cloud, Alexandrov et al. (2012a)), as the polarized signal is generated by single-scattered photons. Knowing the location from where the signal emerges simplifies the interpretation of the result. Furthermore, the cloud top is a highly interesting region, because it is directly affected by entrainment and mixing processes. The polarimetric retrieval stands out because the effective variance of the droplet size distribution is also determined, a parameter, which is directly linked to entrainment and mixing processes.

There are several instruments to which the polarimetric retrieval has been applied successfully, such as POLDER (POLarization and Directionality of the Earth's Reflectances (Bréon and Goloub, 1998; Bréon and Doutriaux-Boucher, 2005; Shang et al., 2019)), RSP (Research Scanning Polarimeter (Cairns et al., 1999; Alexandrov et al., 2012a)), AirHARP (Airborne Hyper-Angular Rainbow Polarimeter (Martins et al., 2018; McBride et al., 2020)) or AirMSPI (Airborne Multi-angle SpectroPolarimetric Imager (Diner et al., 2013)). A detailed overview of various instruments with polarization capabilities that also apply the polarimetric technique is given in McBride et al. (2020).

In 2013 the PODEX campaign took place (Knobelspiesse et al., 2019). This was an extensive intercomparison study between different polarimeters which, e.g., showed that RSP and AirMSPI measurements agree within the expected measurement uncertainties, especially for bright scenes (clouds, land). PODEX was carried out as preparation for the upcoming PACE (Plankton, Aerosol, Cloud, ocean Ecosystem) mission, a polar-orbiting satellite that will deploy two polarimeters for cloud and ocean retrievals (Remer et al., 2019). Alexandrov et al. (2018) compared in situ data to r_{eff} and v_{eff} results from the parametric fit of RSP measurements, and found a good agreement of better than $1\,\mu\mathrm{m}$ for r_{eff} and in most cases better than 0.02 for v_{eff}. Painemal et al. (2021) compared the effective radius and optical thickness of airborne data (polarimetric and bi-spectral retrieval based on RSP measurements and in situ measurements from the Cloud Droplet Probe) with satellite retrievals (MODIS and GOES-13) over the midlatitude North Atlantic. The comparison showed good correlations for the effective radius, but the satellite-based results were systematically higher than the aircraft measurements and the bias was larger for GOES-13 ($5.3\,\mu\mathrm{m}$) than for MODIS ($2.6\,\mu\mathrm{m}$). The discrepancy is partly explained by the high viewing zenith angle of the GOES-13 measurements, and further pixel resolution effects, which both can lead to a positive bias in satellite-derived r_{eff}. Additional factors are the satellite scattering angle and 3-D radiative transfer effects, but these require further investigations. Recently, another comparison study was published by Fu et al. (2022), in which data collected during the Cloud, Aerosol and Monsoon Processes Philippines Experiment (CAMP2Ex) in 2019 were analyzed. One goal of the field campaign was to comprehensively compare r_{eff} retrievals of cumulus clouds from different platforms (MODIS, RSP and in situ). A major advantage is that RSP provides both a bi-spectral and a polarimetric r_{eff} simultaneously without introducing any uncertainties related to co-location. The study shows that the RSP polarimetric, the in situ and the bias adjusted MODIS r_{eff} (Fu et al., 2019) are in good agreement ($9.6\,\mu m$ to $11.0\,\mu m$), but much smaller than the bi-spectral r_{eff} from MODIS ($17.2\,\mu m$) and RSP ($15.1\,\mu m$). For shallow clouds, these differences are primarily caused by 3-D radiative transfer and cloud heterogeneity.

Here, we introduce the polarization upgrade of the airborne camera system specMACS (Ewald et al., 2016) and apply the polarimetric technique to the specMACS measurements. In Section 2 we present the new polarization cameras of specMACS in detail. Compared to other, already established polarimeters like RSP or AirMSPI, which operate in a scanning or pushbroom mode, the specMACS polarization cameras capture a complete 2-D image of the observed scene at a high spatial resolution. The special design of the Sony polarization sensor allows the simultaneous measurement of four different polarization directions and three RGB color channels. The acquired images have a large field of view, which provides frequent observations of the cloudbow. The polarimetric retrieval developed for deriving the cloud droplet size distribution of liquid water clouds is discussed in Section 3 and is applied to specMACS data that were measured during the EUREC^{4}A field campaign in Section 4. We present two case studies: The first one is a stratiform cloud with two cloud layers at different heights. The second case study shows small cumulus clouds (diameters $1\,km$ to $2\,km$). The results are presented as 2-D maps illustrating the high spatial resolution of the specMACS measurements. Section 5 summarizes the results and gives an outlook on planned future work.

2 specMACS Polarization Cameras and Data Processing

The spectrometer of the Munich Aerosol Cloud Scanner (specMACS, Ewald et al., 2016) originally consisted of two hyperspectral line cameras sensitive in the wavelength range from $400\,nm$ to $2500\,nm$. During EUREC^{4}A this set of cameras was for the first time complemented by two polarization-sensitive two-dimensional cameras. All four cameras are built into a pressurized, temperature stabilized, and humidity-controlled housing with a window in front of the cameras. The whole camera system was flown in a nadir looking perspective onboard the German research airplane HALO (Krautstrunk and Giez, 2012). In the past, the hyperspectral cameras have been successfully used to derive cloud droplet radius profiles (Ewald et al., 2019; Polonik et al., 2020) or to retrieve cloud geometry from oxygen-A-band observations (Zinner et al., 2019). In this work, the focus will be on the new polarization cameras.

The two polarimeters are Phoenix polarization RGB cameras (Phoenix 5.0 MP Polarization Model) which come with Sony's IMX250MYR CMOS polarized sensors with 2448 pixels (along track) × 2048 pixels (across track) (LUCID Vision Labs Inc., 2022b). They are accompanied by a Cinegon 1.8/4.8 lens by Schneider-Kreuznach. The aperture is set to 5.6. The two cameras are installed in a partly overlapping perspective which results in a combined maximum field-of-view of about $91°$ (along-track) $\times 118°$ (across-track). This corresponds to a horizontal pixel size at the ground of $10\,m$ to $20\,m$ at a cruise altitude

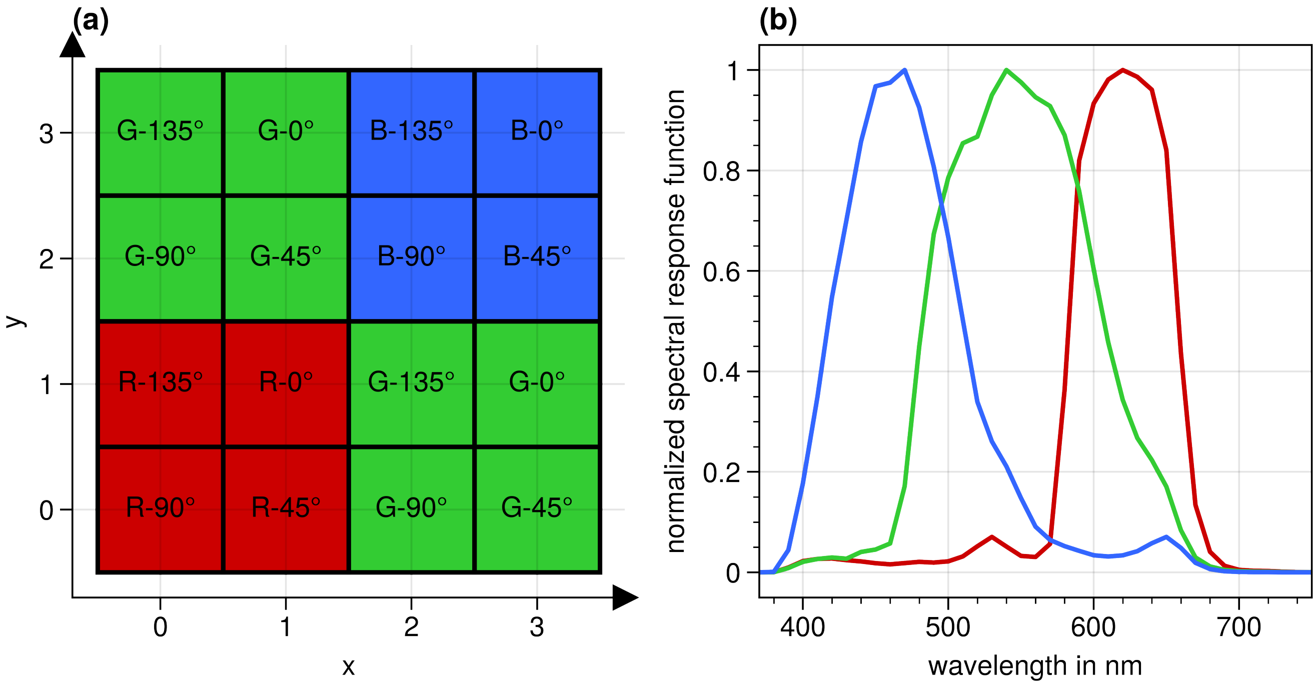

Figure 1. a) Structure of a 4 × 4 pixel block of the polarization cameras. Each 4 × 4 block is sub-divided into four blocks of 2 × 2 pixels for the different colors red (R), green (G), and blue (B). On the 2 × 2 pixel blocks four differently angled polarizers are placed. Figure adapted from the datasheet of the camera. (LUCID Vision Labs Inc., 2022a). b) Normalized spectral response functions of the three color channels averaged over the four polarization directions.

of about $10\,\mathrm{km}$. The cameras are synchronized and measure at an acquisition frequency of $8\,\mathrm{Hz}$. Furthermore, an automatic exposure control system based on the method described in Ewald et al. (2016) is used to adjust the measurements to varying illuminations.

The sensor accomplishes the measurement of polarization with on-chip directional polarizing filters (Fig. 1 a): The 2448 × 2048 pixels are split up into blocks of 4 × 4 adjacent pixels. These blocks are further divided into four 2 × 2 pixel blocks for each color of the color filter array (RGGB - Red, Green, Green, Blue). The normalized spectral response functions of each color channel are shown in Fig. 1 b). Different directional polarizing filters (0°, 45°, 90°, 135°) are placed on top of each pixel (so-called pixelated wire-grid polarizer). This enables the retrieval of three components (I, Q, U) of the Stokes vector of the light. The Stokes vector is a mathematical description of the polarization state of electromagnetic radiation and has four components (Hansen and Travis, 1974):

https://doi.org/10.5194/amt-2022-245
Preprint. Discussion started: 28 September 2022

$$S = \begin{bmatrix} I \\ Q \\ U \\ V \end{bmatrix} = \begin{bmatrix} I_{0^\circ} + I_{90^\circ} \\ I_{0^\circ} - I_{90^\circ} \\ I_{45^\circ} - I_{135^\circ} \\ I_{\text{right-handed polarization}} - I_{\text{left-handed polarization}} \end{bmatrix} \tag{1}$$

I is the total intensity and Q and U describe the linear polarization. The last component of the Stokes vector (V), which cannot be measured by specMACS, specifies the circular polarization. However, circular polarization does not play a role in cloud remote sensing since it is orders of magnitude smaller than linear polarization (e.g. Emde et al. (2015); Hansen and Travis (1974)). The degree of linear polarization (DOLP) describes quantitatively the linear polarization of the light and is defined by DOLP $= \sqrt{Q^2 + U^2}/I$.

Figure 2 displays a measurement from the 2nd Feb 2020. The upper panels show the measurements of the so-called *polA* camera which observes clouds slightly to the left in flight direction, the lower panel corresponds to the *polB* measurements slightly to the right in flight direction. On the left side, the measured total intensities of the two cameras are shown. Dashed lines indicate lines of constant scattering angle. The corresponding degree of linear polarization is shown on the right side of Fig. 2. Most parts of the clouds are unpolarized (dark in the image). The cloudbow region (scattering angle 135° to 165°) and the backscatter glory (scattering angle 170° to 180°) stand out due to their high degree of linear polarization. To avoid interpolation errors, we use the original data from the two individual cameras here, instead of projecting the data into a common mapping/figure.

A Stokes vector is defined with respect to a plane of reference. Often, the scattering plane, which contains both the incoming solar illumination vector and the view vector, is used as a reference plane. This has the advantage, that $U \approx 0$ within the scattering plane and Q contains all information about the polarized signal. In the case of the measurements, the original reference plane is the x-z-plane of the camera coordinate system. The x-axis of the camera coordinate system points into the flight direction which is also the polarizing axis of the 0° filter. The z-axis points in the direction of the optical axis of the camera. For further analysis, each measured Stokes vector is rotated into the scattering plane (Hansen and Travis, 1974) and we only evaluate Q. The window in front of the polarization cameras affects the polarization state of the measurements. To correct for this effect, the window is handled as a linear diattenuator, and the Mueller matrix of a linear diattenuator is applied to the measurements (Bass et al., 1995).

A geometric calibration of the cameras was carried out using the chessboard calibration method described in Kölling et al. (2019) based on Zhang (2000), but we exchanged the thin prism camera model used in Kölling et al. (2019) by the rational model. Both camera models come from the OpenCV library (Bradski, 2000). In order to calculate the pixel coordinates of specific 3-D points, the location and orientation of the camera with respect to a fixed world coordinate system have to be determined. The required precise information about the position and attitude of the aircraft is part of the Basic HALO Measurement and Sensor system (BAHAMAS) dataset. A high precision GNSS aided inertial reference system delivers the data with 100 Hz. The accuracy of the data is further increased by GNSS post processing after the flight (Giez et al., 2021). The camera location

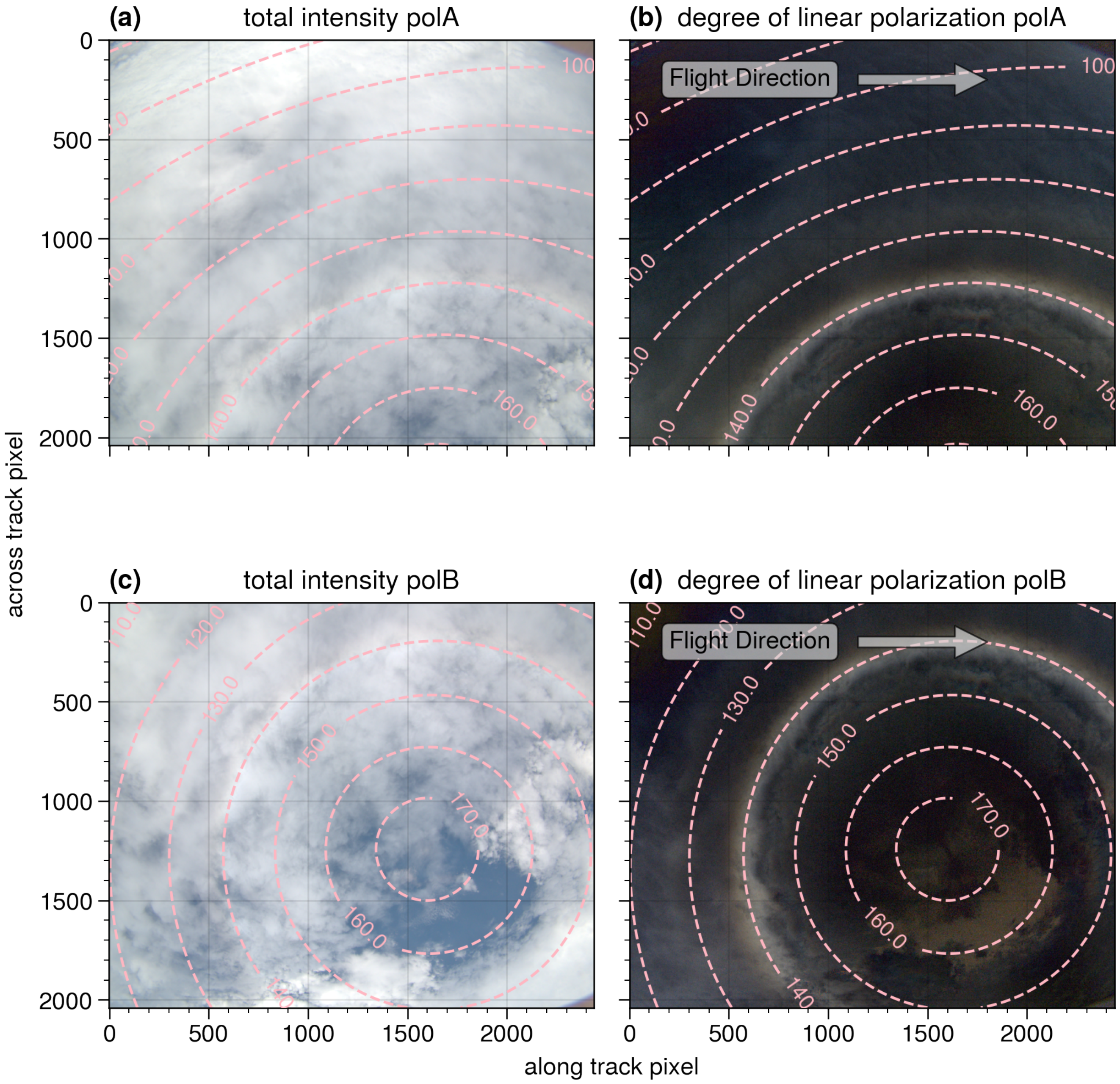

Figure 2. Example of measurements of both polarization cameras (2020-02-02 16:47:45.07 UTC). Top: Measurements from the first polarization camera (*polA*). This camera looks slightly to the left in flight direction. Bottom: Measurements from the second polarization camera (*polB*) which looks slightly to the right in flight direction. The field-of-view of the two cameras overlaps. Left: total intensity, right: degree of linear polarization. The dashed lines indicate lines of constant scattering angles in degree. The cloudbow is visible in the degree of linear polarization as a bright bow at a scattering angle of about 140°

and orientation relative to the airframe is determined from the measured aircraft position and the location of distinct features like rivers or roads in the images once after installation.

3 Retrieval Description

The goal of our algorithm is to determine the size distribution of cloud droplets from (angularly resolved) cloudbow measurements. An average cloudbow signal can be extracted from a single measurement (e.g., from Fig. 2) by radial averaging the data. This method can easily be applied to any cloudbow observations, including those from commercial cameras, but it requires averaging over a large area. With HALO, we fly over the clouds at a speed of about $200\,\mathrm{m\,s^{-1}}$, observing the same cloud from different viewing directions. This allows for a more sophisticated approach which is illustrated in Fig. 3. Instead of evaluating the cloudbow in individual images, different viewing directions are sampled for each target on the cloud as we fly over it. Similar approaches were also applied to measurements of other airborne and space-borne instruments (e.g., Bréon and Goloub (1998); Alexandrov et al. (2015); McBride et al. (2020). The retrieval consists of three steps: First, cloud surface locations ("cloud targets") in the real world 3-D space and their trajectory caused by the wind are determined. 10×10 pixels are combined to form a target pixel with a size of about $100\,\mathrm{m} \times 100\,\mathrm{m}$. Second, for each of these cloud targets, the pixels of all images observing that location are collected. The individual measurements of one target are aggregated into a combined radiance measurement for the entire range of the viewing directions. In a final step, a look-up table (LUT) of cloudbow signals for different cloud droplet size distributions is fitted to the angular distributions, to retrieve the best fitting cloud droplet size distributions. The particular steps of the aggregation process and the retrieval are described in the following.

3.1 Cloud Detection

The first step of the algorithm consists of detecting clouds in the measurements. As most measurements were taken above the ocean, the measurements are often contaminated with sunglint which appears due to the specular reflection of sunlight at the ocean. Cloud detection algorithms based on the brightness of the image often wrongly identify this bright sunglint as clouds. To (partially) overcome this problem we use the parallel component of the polarized light for the cloud detection: The reflectance of the sunglint is significantly reduced in the parallel component. At the Brewster angle ($\theta_B \approx 53.1°$ for an air-water interface) reflected light is even completely perpendicularly polarized (Bass et al., 1995). In the case of a scene with medium cloud coverage, the algorithm chooses the red channel of the parallel component for further processing. For scenes with high cloud coverage, the normalized red (r) blue (b) ratio (nrbr $= (b_{\parallel} - r_{\parallel})/(b_{\parallel} + r_{\parallel})$) is calculated. Based on a brightness histogram of the selected data, a threshold value that distinguishes between cloudy and cloud-free pixels is determined with the method described in Otsu (1979).

All cloudy pixels are further filtered: A cloudy pixel is suitable for the cloudbow algorithm if it is observed within all scattering angles from 135° to 165° during the measurement sequence (for the choice of the range see, e.g., Alexandrov et al. (2012a); McBride et al. (2020)). This of course depends on the solar geometry and the camera's viewing direction. Therefore, the next step is to identify the cloud targets that meet this criterion. In the case of Fig. 2, the upper part of the measurement

https://doi.org/10.5194/amt-2022-245
Preprint. Discussion started: 28 September 2022

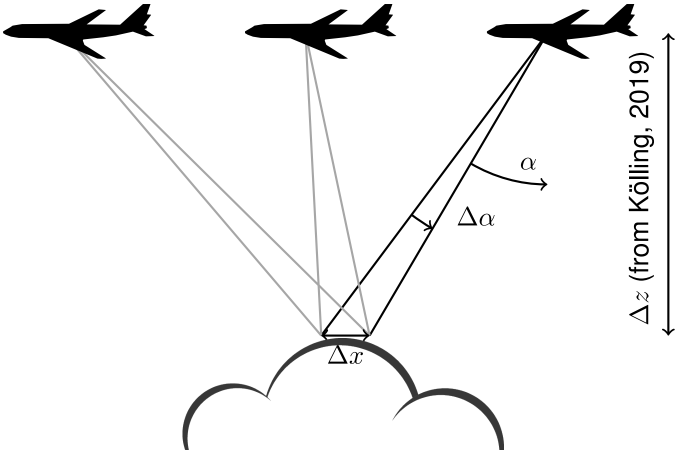

Figure 3. Observation geometry: The same target on the cloud (indicated by Δx) is observed from different viewing angles (α). The cloud top height information needed to calculate the distance Δz between target and camera is retrieved using the method described in Kölling et al. (2019). The single measurements are then aggregated into one radiance measurement of the target.

cannot be used for the cloudbow retrieval as these clouds are not observed from the full scattering angle range needed while the aircraft is flying above the cloud. The flight direction is to the right as indicated by the arrow in Fig. 2 and the scattering angles are shown as dashed, circular lines.

3.2 Geolocalization of cloud targets

In order to identify the same target in different observations, we first use the geometric calibration of the camera to determine the viewing angle of the target (see Section 2). To fully localize the target we need to know the distance between the aircraft and the target (Δz in Fig. 3). The altitude of the airplane and thus from the camera is measured by the BAHAMAS system. The cloud top height is derived using a stereographic reconstruction method which determines the cloud geometry of specMACS measurements. This was demonstrated for measurements of the previous 2D RGB camera in Kölling et al. (2019). The method identifies pixels with prominent features which are detected in the following images by a matching contrast. To correct for horizontal displacements of the cloud, the method was extended to include data of the horizontal wind from ERA5 (Hersbach et al., 2020, 2018).

Figure 4 a) shows an example of the derived cloud top height of the *polB* camera using the stereographic method for the scene shown in Fig. 2 c) and d) (2020-02-02 16:47:45 UTC). Although the method has difficulties for homogeneous regions of the cloud due to a lack of contrasts (e.g., in the lower right), large parts of the cloud are analyzed successfully. The cloud top heights from the single points of the stereographic method are interpolated onto the whole image (Fig. 4 c) and assigned to the selected cloud targets. The WALES lidar system was also operated onboard HALO during EUREC^{4}A (Wirth et al., 2009; Konow et al., 2021). The stereographically derived cloud top height is very similar to the measured cloud top height from the WALES lidar which is projected onto the specMACS RGB image in Fig. 4 b) (Wirth, 2021). Panel c) plots the WALES track on top of the interpolated specMACS cloud top height map. Within the high cloud on the left, the WALES data agree very well with the specMACS cloud top height and it is hard to distinguish the WALES data from the stereo data. The two datasets differ for the cloud on the right, where the stereo result is approximately $1000\,\mathrm{m}$ lower than the lidar measurement. From the videos of the specMACS measurements, it can be seen, that the two cloud layers are mostly adjacent to each other, not on top of each other, but overlap slightly at the cloud edges. specMACS detects the lower cloud layer due to greater contrasts, while WALES is sensitive to the upper cloud layer. This behavior was also observed in Kölling et al. (2019). The yellow rectangle in panel c) indicates a cutout region of the specMACS data, that roughly surrounds the WALES track. These data are shown in the probability density (panel d) in yellow. The cloud top heights of the two cloud layers are at approximately $2700\,\mathrm{m}$ and $1700\,\mathrm{m}$ (Fig. 4 d). The distribution of the interpolated stereo points is quite similar to the distribution of the WALES data (shown in blue), even though the two datasets differ for the cloud on the right.

Even a small error of a few hundred meters in the cloud top height will result in an erroneous localization of the cloud in subsequent images. An incorrect localization particularly affects targets close to cloud edges, where it will cause non-cloud regions to be aggregated into the final cloudbow signal. Luckily, the stereographic method can very accurately determine the cloud geometry at cloud edges due to high contrasts.

By combining the cloud top height with the viewing directions, the locations of the cloud targets in the real world 3-D space are determined. These are used to calculate the pixel coordinates of the targets in successive measurements (Fig. 3), again considering the shift with the wind of the targets. The individual measurements of the same target of the Stokes parameter Q are combined to generate the aggregated radiance measurement. For further processing, the radiance measurement is binned onto a scattering angle grid with a step size of $0.3°$.

3.3 Size distribution retrieval

Polarized measurements are dominated by single scattering (Hansen, 1971). In general, any scattering process is described by the so-called scattering matrix or phase matrix which relates incident to scattered radiation (Hansen and Travis, 1974). The scattering matrix is a 4×4 matrix with matrix elements P_{ij}. The P_{12} element is also called the polarized (single scattering) phase function and is a good approximation for the measured polarized radiance Q (Bréon and Goloub, 1998). Figure 5 shows examples of the polarized phase function for different effective radii (a) and different effective variances (b). This figure illustrates how the properties of the cloud droplets determine the shape and structure of the phase function, and thus the radiance within the cloudbow and glory region. The position of the maxima and minima of the polarized phase function strongly depends on the effective radius (left figure). The effective variance, however, determines the number of secondary minima of the radiance distribution but has only a small effect on the position of the minima. Analysing the backscatter

https://doi.org/10.5194/amt-2022-245
Preprint. Discussion started: 28 September 2022

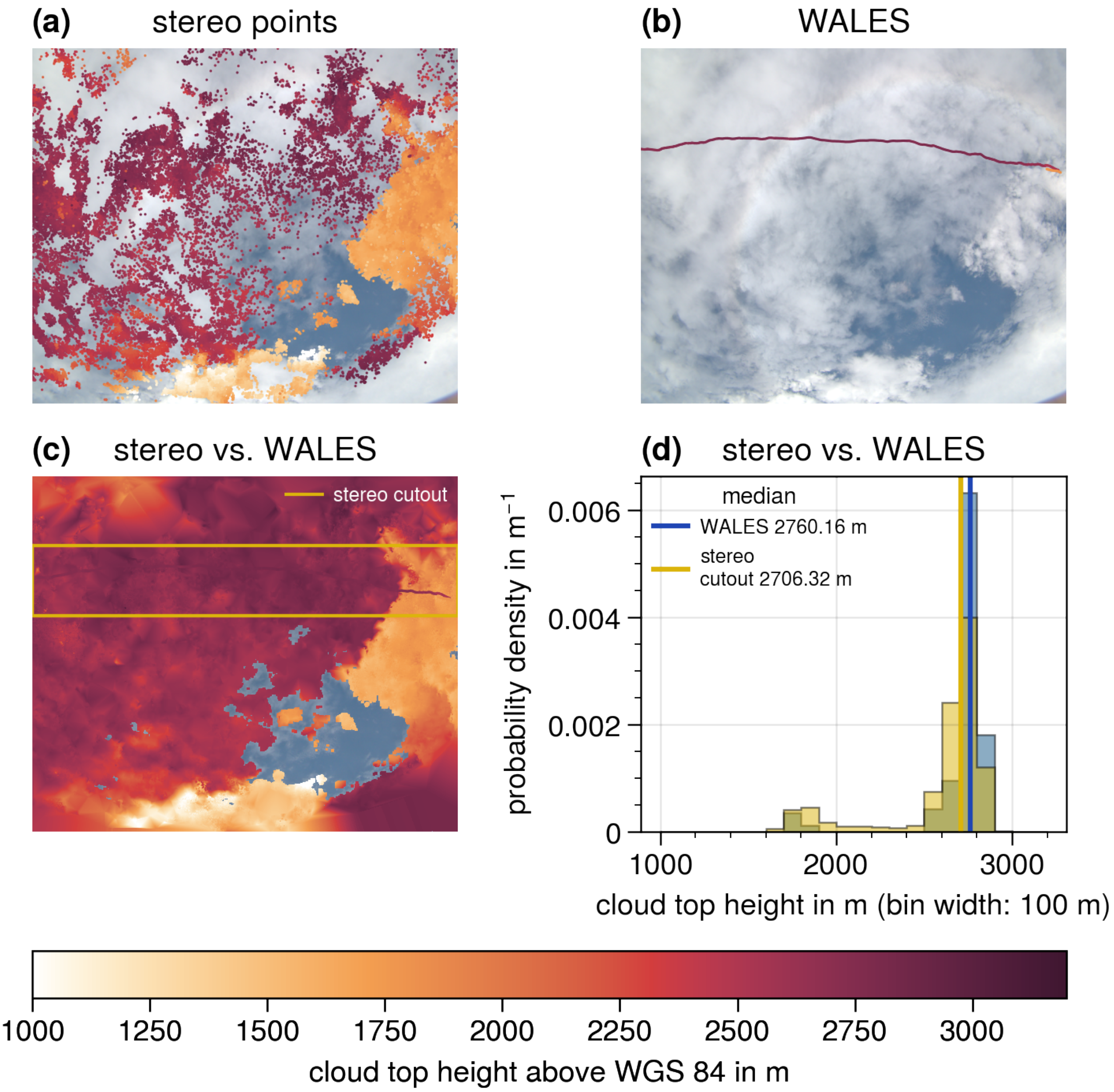

Figure 4. Cloud top height (CTH) information of the cloud field shown in Fig. 2 (2020-02-02 16:47:45.07 UTC): a) CTH of stereo points from the stereographic reconstruction method; b) CTH from the WALES lidar system; c) Interpolated CTH based on the stereo points. The WALES CTH is plotted on top and the yellow rectangle indicates a specMACS cutout surrounding the WALES track. Panel d) shows the probability densities of the CTHs of the specMACS cutout (yellow) and the WALES measurements (blue). The RGB measurement of the cloud field is shown in the background of the panels a), b), and c). The colorbar at the bottom corresponds to all cloud top height measurements shown in the panels a), b) and c).

https://doi.org/10.5194/amt-2022-245
Preprint. Discussion started: 28 September 2022

glory is an extremely accurate method to retrieve r_{eff} and v_{eff} (Spinhirne and Nakajima, 1994; Mayer et al., 2004). But the glory requires a special observation geometry, and can therefore only be evaluated for a small fraction of the image area. The cloudbow however, covers a large area and thus is easier to observe, while still depending strongly on the size distribution.

For evaluating the aggregated angular radiance measurement with regard to the cloud droplet size properties (see Fig. 5), a LUT of polarized phase functions (P_{12}) for different effective radii and different effective variances was created for each of the three spectral color channels of the camera. All calculations were carried out with the Mie Tool of the library for radiative transfer (libRadtran) (Wiscombe, 1980; Mayer and Kylling, 2005; Emde et al., 2010, 2016). We assume that the cloud droplet size distribution has the shape of a gamma distribution. This is an extensively used assumption (Alexandrov et al., 2015), which is, e.g., confirmed by in situ measurements of liquid water cloud droplet size distributions (e.g., Miles et al., 2000). The effective radius and the effective variance of any cloud droplet size distribution are defined as (Hansen, 1971):

1. Effective radius

$$r_{\text{eff}} = \frac{\int_0^\infty r\pi r^2 n(r)dr}{\int_0^\infty \pi r^2 n(r)dr} \tag{2}$$

2. Effective variance

$$v_{\text{eff}} = \frac{1}{r_{\text{eff}}^2}\frac{\int_0^\infty (r-r_{\text{eff}})^2\pi r^2 n(r)dr}{\int_0^\infty \pi r^2 n(r)dr} \tag{3}$$

Here, r is the droplet radius and $n(r)$ is the droplet size distribution. The formula of the gamma distribution can be written as a function of r_{eff} and v_{eff} (Hansen, 1971):

$$n_\gamma(r) = n_0 r^{(1-3v_{\text{eff}})/v_{\text{eff}}} \exp^{[-r/(r_{\text{eff}}v_{\text{eff}})]} \tag{4}$$

with:

$$n_0 = \frac{N(r_{\text{eff}}v_{\text{eff}})^{[(2v_{\text{eff}}-1)/v_{\text{eff}}]}}{\Gamma(\frac{1-2v_{\text{eff}}}{v_{\text{eff}}})}, \tag{5}$$

where N is the total number of particles per unit volume. In Fig. 5 c) and d) several gamma distributions for different v_{eff} (c) and r_{eff} (d) are shown.

Polarized phase functions are calculated for a logarithmic grid of 77 different effective radii ranging from $1\,\mu\text{m}$ to $40\,\mu\text{m}$ ($r_{\text{eff, i+1}} = r_{\text{eff, i}} \cdot 1.05$). The effective variances range between 0.01 and 0.32 with a small step size of 0.01 for $v_{\text{eff}} \leq 0.05$, and a larger step size (0.02 to 0.028) for $v_{\text{eff}} > 0.05$. This choice is similar to other publications such as Alexandrov et al. (2012a); McBride et al. (2020). In total, the LUT includes 16 different effective variances. To account for the different spectral sensitivities of the three color channels, the polarized phase functions are initially calculated for the whole wavelength range of the spectral response functions with a step size of $10\,\text{nm}$, and are then weighted by each spectral response function (Fig. 1 b). For the calculation of the phase functions, a wavelength and temperature-dependent refractive index is used. We use the

https://doi.org/10.5194/amt-2022-245
Preprint. Discussion started: 28 September 2022

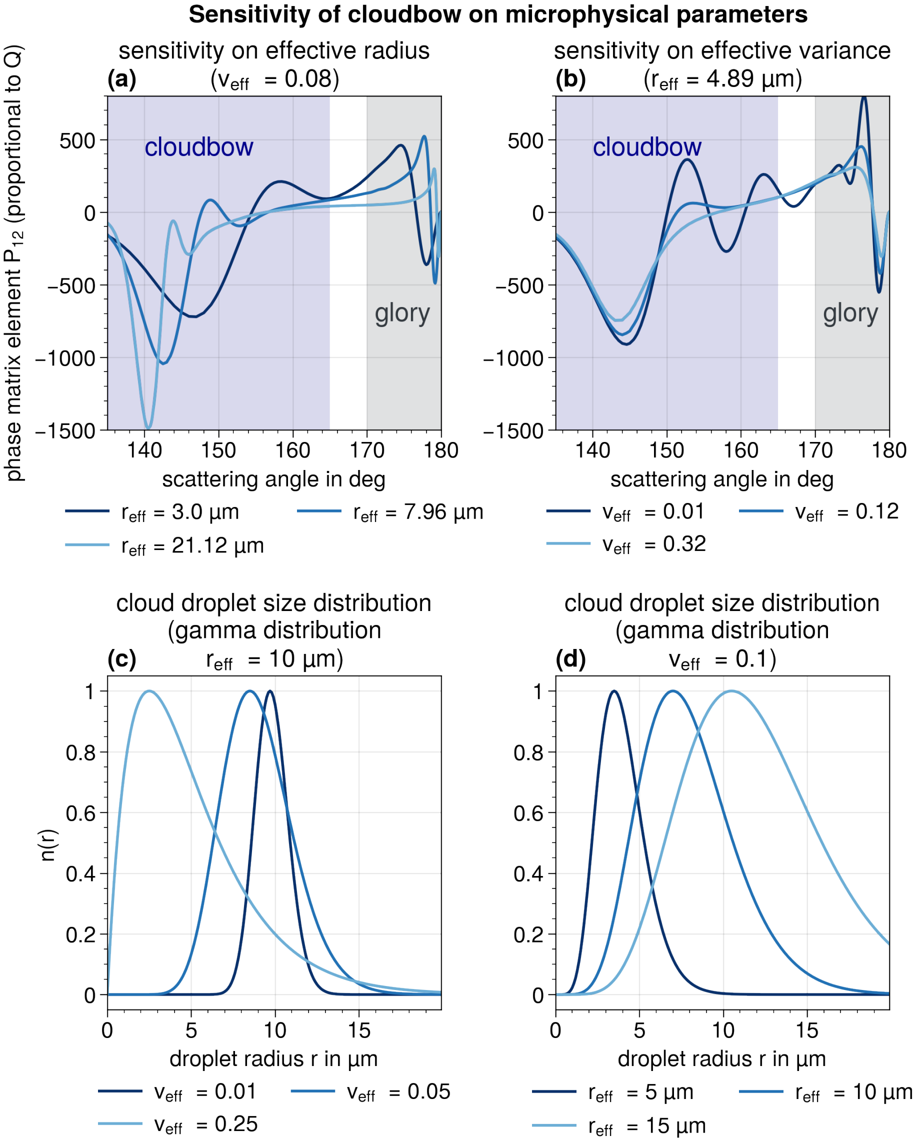

Figure 5. Sensitivity of cloudbow on microphysics. Plot a) shows that the cloudbow signals (P_{12}) vary if the effective radius is changed while the effective variance is constant (v_{eff} = 0.08). Plot b) illustrates the effect of a change in the effective variance while the effective radius is held constant ($r_{eff} = 4.89\,\mu m$). For calculating P_{12}, we assume, that the cloud droplet size distribution has the shape of a gamma distribution. In the plots c) and d), several gamma distributions for different effective variances and a constant $r_{eff} = 10\,\mu m$ (c) and for different effective radii and a constant $v_{eff} = 0.1$ (d) are shown.

https://doi.org/10.5194/amt-2022-245
Preprint. Discussion started: 28 September 2022

approximation formula of the IAPWS (International Association for the Properties of Water and Steam, Wagner and Pruß (2002)) for a temperature of $T = 10\,^\circ\mathrm{C}$ which, according to dropsondes measurements, corresponds to the approximate cloud top temperature of the typical EUREC^{4}A clouds with a cloud top height of $1700\,\mathrm{m}$.

The LUT of polarized phase functions ($P_{12}[r_\mathrm{eff}, v_\mathrm{eff}]$) is fitted to the aggregated radiance distributions (Q_meas) using the following equation:

$$Q_{fit}(\theta) = A \cdot P_{12}[r_\mathrm{eff}, v_\mathrm{eff}](\theta) + B \cdot \cos^2(\theta) + C \tag{6}$$

Here, A, B and C are fitting parameters and θ is the scattering angle. Parameter A is needed to compare the radiometrically uncalibrated measurements with the simulated LUT, and, in addition, scales with the cloud fraction of the target made up of 10×10 pixels (Bréon and Goloub, 1998). The fitting parameters B and C account for errors from any remaining effects that are not considered in the single scattering assumption. For example, these could be contributions by multiple scattering. The term $\cos^2(\theta)$ corrects for Rayleigh scattering contributions (Alexandrov et al., 2012a). To determine P_{12}, and thereby the effective radius and effective variance of the cloud droplets, a least-squares approach is used to invert Equation 6. In the inversion process, not only the grid points of the LUT are allowed, but also values in between. This is realized by a linear interpolation of the LUT. The root mean square error (RMSE) is calculated for the scattering angle range from 135° to 165° where the cloudbow structure is most prominent:

$$\mathrm{RMSE} = \sqrt{\frac{1}{n}\sum_{i=1}^{n}(Q_\mathrm{fit}(\theta_i) - Q_\mathrm{meas}(\theta_i))^2} \tag{7}$$

The smallest RMSE reveals the effective radius and effective variance of the cloud droplets. In addition, the RMSE serves as a measure of accuracy. As a second quality measure, we calculate the so-called quality index (Qual, first defined by Bréon and Doutriaux-Boucher (2005)). This is the ratio between the variability of the measurement, which corresponds to the squared amplitude of the cloudbow ($A \cdot P_{12}$), and the RMSE of the fit (see Equation 8). Measurements with a low quality index ($\mathrm{Qual} < 2$) are filtered out of any further processing. This excludes, for example, "cloudbow signals" of ocean areas that have been incorrectly identified as clouds from the result.

$$\mathrm{Qual}^2 = \frac{A^2(\langle P_{12}^2\rangle - \langle P_{12}\rangle^2)}{\mathrm{RMSE}} \tag{8}$$

Figure 6 shows two examples of aggregated cloudbow measurements for the green channel (boxes, frequency indicated by color) binned into 0.3° resolution in scattering angle (black dots with standard deviation and connecting black line). Each corresponding model fit is plotted as a solid, yellow line. The model fit matching example a) has an $\mathrm{r_{eff}}$ of $17.63\,\mu\mathrm{m}$ and an $\mathrm{v_{eff}}$ of 0.08. Example b) has an $\mathrm{r_{eff}}$ of $5.98\,\mu\mathrm{m}$ and an $\mathrm{v_{eff}}$ of 0.08.

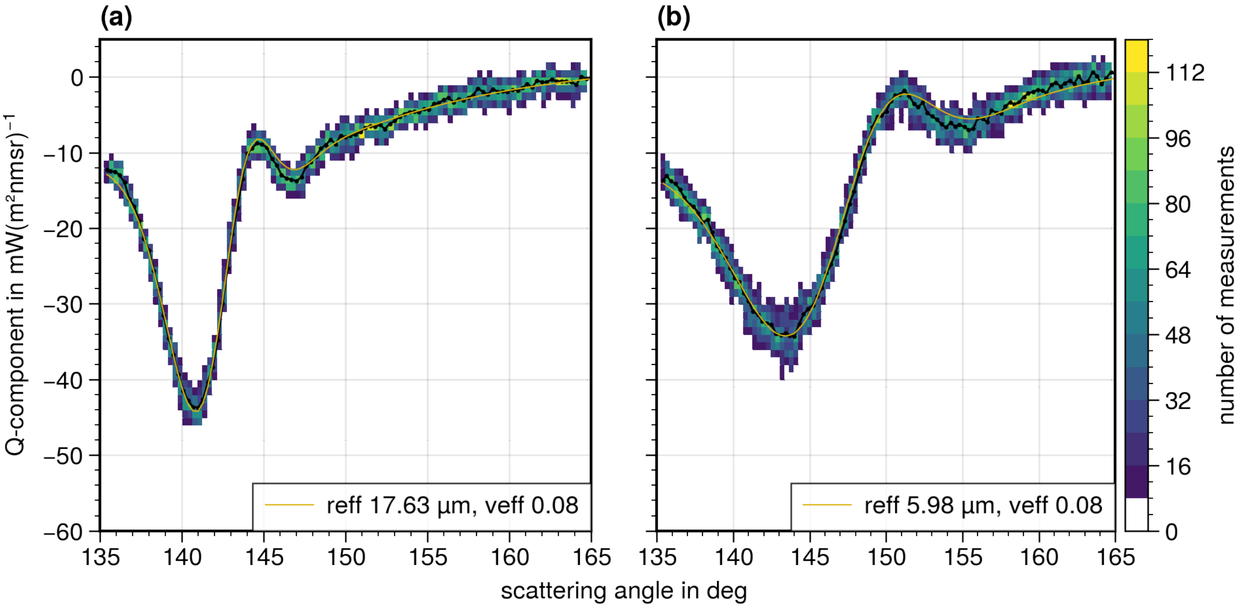

Figure 6. The two panels show the aggregated polarized radiance measurements of the green channel of two different target regions. The measurements were binned into small boxes with a vertical size of $1\,\mathrm{mW\,m^{-2}\,nm^{-1}\,sr^{-1}}$ and a horizontal size of $0.3°$. The number of measurements within a box is indicated by the color of the box. Furthermore, the raw data are binned to $0.3°$ resolution in scattering angle (black dots connected by black lines). The yellow lines indicate the best fitting simulations. The parameters r_{eff} and v_{eff} of the best fitting simulations are shown in the boxes in the lower right.

4 Retrieval Results

In the following, two case studies of the 2nd February 2020 are presented. On this day the observed clouds had a clear Flower organisation (Stevens et al., 2020). Such cloud fields are characterized by shallow trade-wind cumuli organized into large, stratiform clusters ($20\,\mathrm{km}$ to $200\,\mathrm{km}$) with high rain rates, surrounded by a large clear-sky region (Stevens et al., 2020; Schulz et al., 2021). Among the four named mesoscale cloud patterns (Flower, Gravel, Fish, Sugar), the Flower clouds have the highest cloud radiative effect (Bony et al., 2020), mostly because of their large low level cloud fraction. We demonstrate the polarimetric technique based on two case studies from specMACS measurements of this day. The first case study shows a part of the (stratiform) Flower structure. In the second example we analyze small trade wind cumuli which were connected to a cold pool that formed during the dissipation of the Flower. We limit the presentation of the retrieval results to the green channel, as the results from the red and blue channel are very similar.

4.1 Case Study 1 – Stratocumulus Flower Cloud System

First, we present the Flower cloud observed at 16:47:45 UTC. This measurement was already introduced in Section 3 and was shown in Fig. 2. At this time, HALO was flying at an altitude of about $10\,\mathrm{km}$ and the solar zenith angle was $31.15°$. The cloudbow technique is applied to the measurements. The time required to sample the angular range $135°$ to $165°$ is $40\,\mathrm{s}$. The retrieval results of the individual cloud targets are combined into maps of $\mathrm{r_{eff}}$ and $\mathrm{v_{eff}}$ (Fig. 7). About one third of the image can be evaluated, as only the targets inside this area are observed from all necessary scattering angles during the overpass.

The map of $\mathrm{r_{eff}}$ (Fig. 7 a) is a consequence of the vertical distribution of the cloud field with two cloud layers at different cloud top heights (Fig. 4). Due to the high spatial resolution of the specMACS measurements, clear features of the spatial distribution are revealed: The upper cloud deck at a cloud top height of about $2650\,\mathrm{m}$ has a large $\mathrm{r_{eff}}$ ranging between $15\,\mathrm{\mu m}$ and $40\,\mathrm{\mu m}$. Distinct patches of very large $\mathrm{r_{eff}}$ values up to $40\,\mathrm{\mu m}$ are observed. These patches occur in regions where the cloud is optically thick (Fig. 7 d). The spatial distribution of $\mathrm{r_{eff}}$ of the lower cloud deck (cloud top height at $1700\,\mathrm{m}$) is more homogeneous and the absolute values are much smaller ($\mathrm{r_{eff}} \approx 6\,\mathrm{\mu m}$). Figure 7 c) shows the frequency distribution of $\mathrm{r_{eff}}$. Here, the two peaks of $\mathrm{r_{eff}}$ of the two cloud decks are very well distinguishable. The retrieved $\mathrm{r_{eff}}$ values of the higher cloud are very large. This finding is confirmed by high reflectivity values of the polarimetric $\mathrm{K_a}$-band MIRA-35 cloud radar measurements of the HAMP instrument (Mech et al., 2014; Konow et al., 2021). The radar measurements from 16:47:00 to 16:48:30 UTC are shown in Fig. 8 along with a push-broom like image of the specMACS measurements and an indication of the HAMP radar field of view within the specMACS image. Within the high cloud from 16:47:00 to 16:48:15 the radar shows bands of enhanced reflectivity > 0 dBz. This corresponds to falling, and thus large droplets, which confirms our result of large effective radii.

For our polarimetric technique, it is necessary to make an assumption on the shape of the cloud droplet size distribution. Currently, we use a monomodal gamma distribution. In reality, if precipitation starts to develop, a tail in the cloud droplet size distribution begins to form. Especially during the first stage of precipitation formation, a lot of drizzle cloud droplets are apparent inside the clouds, leading to a bi-modal size distribution. In Alexandrov et al. (2012b) it was shown that for clouds with a bi-modal size distribution (e.g., due to drizzle), the polarimetric retrieval based on monomodal size distributions is biased towards the dominant mode. To overcome this problem, the rainbow fourier transformation (RFT) was developed (Alexandrov et al., 2012b), that retrieves the cloud droplet size distribution without any assumptions on the number of modes of the distribution (Alexandrov et al., 2012b). In Sinclair et al. (2021) observations of stratiform clouds measured with the RSP are evaluated using the RFT. The analysis shows a bi-modal droplet size distribution, from which precipitation rates are estimated. These are strongly correlated to radar derived rainwater paths and precipitation rates. We plan to apply this approach also to specMACS measurements in future.

Although our results might be biased due to the existence of a second mode in the cloud droplet size distribution, the statement, that the maps show extraordinary large effective radii is still valid. The retrieved $\mathrm{r_{eff}}$ give a lower limit of the actual $\mathrm{r_{eff}}$, following the argumentation from above. To our knowledge, this is the first time, that such large $\mathrm{r_{eff}}$ are retrieved from the polarimetric technique and presented in a study. This case study is particularly interesting, as the retrieved effective radii lie within the so-called size gap where neither the diffusional growth, nor growth by collision-coalescence is effective (Grabowski

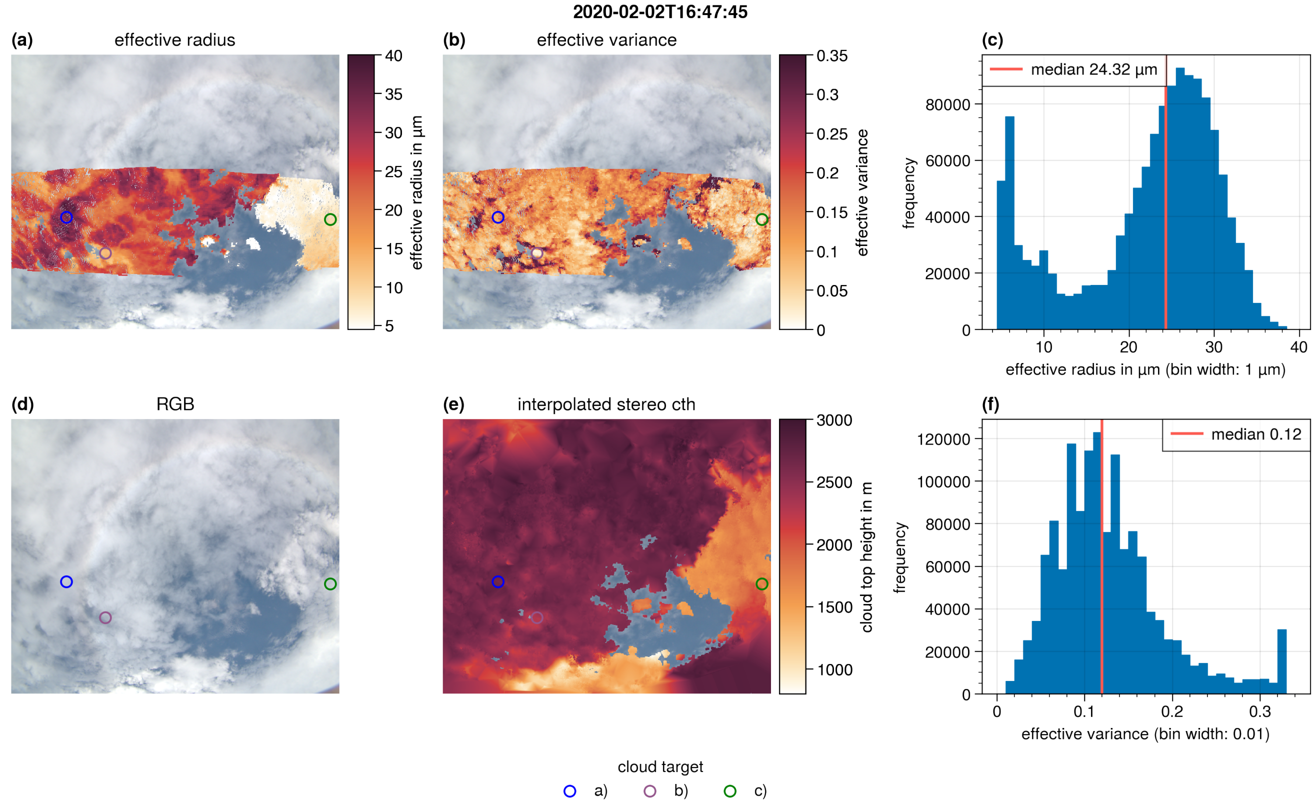

Figure 7. Spatial distribution of effective radius (left) and effective variance (right) for the case study presented in Fig. 2. The retrieval is applicable to the area observed within 135° to 165° in scattering angle by aggregating successive images. Three specific targets are indicated by colored circles.

and Wang, 2013). When comparing the polarimetric technique to the traditional bi-spectral retrieval, it should be noted, that the same issue persists for bi-spectral retrievals, as these are (normally) also based on simulations with monomodal cloud droplet size distribution (Platnick et al., 2017) leading to an underestimation of the true r_{eff}, although this effect seems to be rather small (Zinner et al., 2010; Zhang et al., 2012).

The spatial distribution of v_{eff} in Fig. 7 b) does not show a clear separation of the two cloud decks. Again, small defined patches of both very high and very small v_{eff} can be seen. At the boundary between the two cloud decks, large v_{eff} values are observed over several pixels. These are the result of a mixing of the signals of the two different cloud decks with different cloud droplet size distributions. Similar effects were seen in RSP observations of multi-layer clouds (Alexandrov et al., 2015, 2016). The resulting oscillating signal cannot be reproduced by a mono-modal polarized phase function, and the outcoming fit has a large effective variance. The frequency distribution of v_{eff} is shown in Fig. 7 f). The distribution has two prominent peaks, one at about 0.1 and the other at 0.32, the upper limit of the LUT. This indicates that the LUT should be expanded for larger

https://doi.org/10.5194/amt-2022-245
Preprint. Discussion started: 28 September 2022

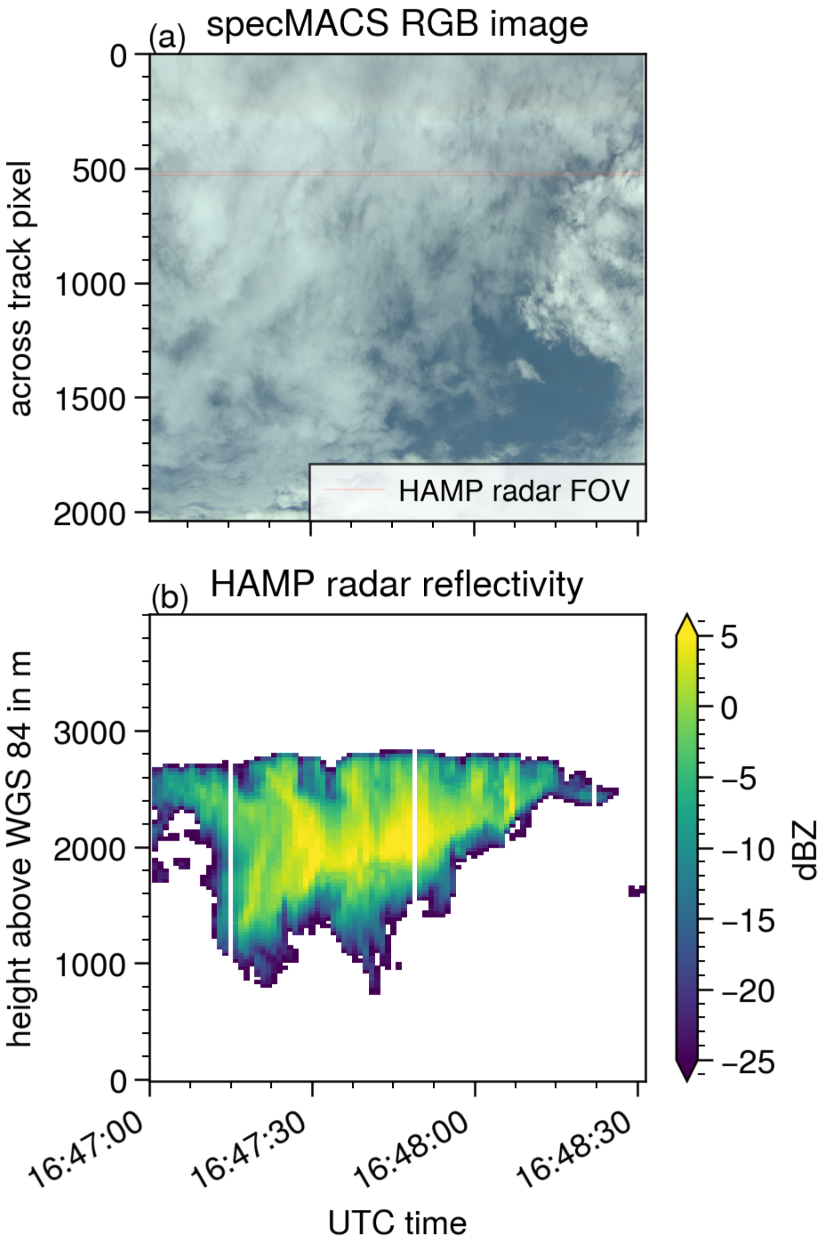

Figure 8. Temporal evolution of specMACS measurement (a) and HAMP radar reflectivity (b) for case study 1. The specMACS measurements are stacked together from individual images to generate a push-broom like image with a time axis. The HAMP radar field of view is marked within the specMACS image.

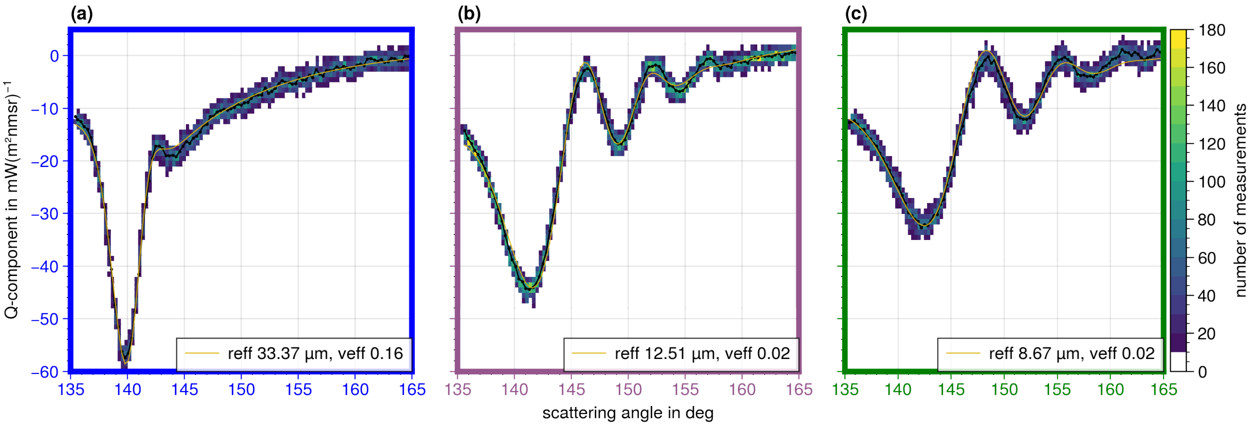

Figure 9. The aggregated polarized radiance measurements of the green channel of the locations shown in Fig. 7 were binned into small boxes with a vertical size of $1\,\mathrm{mW\,m^{-2}\,nm^{-1}\,sr^{-1}}$ and a horizontal size of 0.3°. The number of measurements within a box is indicated by the color of the box. Furthermore, the raw data are binned to 0.3° resolution in scattering angle (black dots connected by black lines). The yellow lines indicate the best fitting simulations. The parameters $\mathrm{r_{eff}}$ and $\mathrm{v_{eff}}$ of the best fitting simulations are shown in the boxes in the lower right.

$\mathrm{v_{eff}}$ values which correspond to broad size distributions. For broad size distributions, however, the features of the cloudbow are smoothed out which makes the retrieval less robust.

Small cracks are visible within the spatial distributions of $\mathrm{r_{eff}}$ and $\mathrm{v_{eff}}$ due to the reprojection of the targets onto the RGB image of the measurement, as there are small discontinuities within the interpolated stereo cloud top height. This in turn results in discontinuities within the locations of the reprojected targets.

The maps in Fig. 7 contain indicators of three particular cloud targets. For these targets, the respective aggregated cloudbow measurements are plotted together with the model fits in Fig. 9. The targets a) and b) both lie within the high cloud deck. Target a) is located within a patch of very high $\mathrm{r_{eff}}$. The corresponding cloudbow measurement has one very sharp minimum, and a second, weaker one. This indicates a relatively broad cloud droplet size distribution. This is confirmed by the quite large $\mathrm{v_{eff}}$ value of 0.16. The measurement of target b) has several secondary minima. $\mathrm{v_{eff}}$ is therefore reduced compared to target a) ($\mathrm{v_{eff}}$ = 0.02). Target c) lies within the lower cloud deck. The cloudbow minimum is shifted to slightly larger scattering angles and the amplitude of the cloudbow is smaller than the amplitudes of targets a) and b). According to our expectations from the simulations (Fig. 5), this corresponds to a smaller $\mathrm{r_{eff}}$, which is confirmed by the fit ($\mathrm{r_{eff}}$ = $8.67\,\mu\mathrm{m}$). The existence of the secondary minima indicates a narrow size distribution which is verified by the small effective variance of the fit ($\mathrm{v_{eff}}$ = 0.02). All three measurements have only little noise.

4.2 Case Study 2 – Small Cumulus Clouds

In the following subsection, a second case study is discussed. The observations were taken from 18:28:15 UTC to 18:31:30 UTC. HALO was flying at an altitude of $10\,345\,\mathrm{m}$ and the solar zenith angle was $46.1°$. The measurement shows a cloud field of small trade wind cumulus clouds with diameters of about $1\,\mathrm{km}$ to $2\,\mathrm{km}$ (Fig. 10 b).

We are choosing this example, to demonstrate that the retrieval is capable of generating good results even in the case of more heterogeneous cloud scenes, and especially for small cumulus clouds. In such scenes, the traditional bi-spectral retrieval has issues with three dimensional radiative transfer effects (Marshak et al., 2006). These are, e.g., shadowing or illumination effects, which are normally not accounted for in standard radiance look-up tables.

In the case of such small cumulus clouds, a precise geolocalization of the cloud targets is very important to correctly track targets in consecutive images. This geolocalization depends on three factors: First, the internal calibration of the camera, second, the (mainly horizontal) wind at the cloud top, and third, the retrieved cloud top height. In the following we argue that, while these points certainly cause uncertainty in the geolocalization, they affect the cloudbow retrieval only by a lesser degree.

The internal calibration was verified using known targets at the ground: A slight deviation from the actual target of less than $100\,\mathrm{m}$ was observed, which also varied during the overflight. A possible reason for a slightly varying offset could be a degrading heading accuracy of the inertial reference system on long straight flight legs with no heading variation (Giez et al., 2021). As most of the EUREC^{4}A flights were conducted on a circular flight pattern, the heading of the airplane continuously changed and the accuracy of the position and attitude data is very high. Since the inertial reference system is located in the nose of the airplane and the specMACS system in the tail, deformation of the fuselage caused by air turbulence or outside pressure change could also induce a varying offset in the pointing accuracy. Other inaccuracies result from the geometric chessboard calibration of the cameras and from the determination of the correct position of the specMACS instrument relative to the airframe by aligning specMACS measurements with satellite imagery. Based on this analysis of known ground targets, we used cloud targets of a size of $100\,\mathrm{m}$ by $100\,\mathrm{m}$ in the current study. Future work will address improving the geometric calibration of the cameras to allow the study of even smaller targets.

The second factor that affects the geolocalization is the ambient horizontal wind. We apply a wind correction to the initial location of the cloud target to account for any drift due to the wind, and explain, why this is necessary in the following. According to the ERA5 data, the ambient horizontal wind of the case study at the cloud height (about $1\,\mathrm{km}$) was an east-southeast wind (direction $103.35°$) with a wind speed of about $6\,\mathrm{m\,s^{-1}}$. This is also confirmed by dropsondes measurements. During the flight, it took about $35\,\mathrm{s}$ to sample the targets from the angular range 135° to 165°. During this aggregation process, a target cloud shifts by $210\,\mathrm{m}$ due to the wind. For a cloud target with a size of about $100\,\mathrm{m} \times 100\,\mathrm{m}$ this means that it moves further by more than two target units, therefore a wind correction is required. In addition, a cloud can evolve significantly within $35\,\mathrm{s}$, especially in the very active region at the cloud boundary, where the cloud grows or shrinks depending on cloud dynamics and the interaction with the environment.

The stereographic cloud geometry retrieval is very well applicable to this cloud field because of the strong contrasts between the clouds and the ocean. The resulting cloud top height (shown in Fig. 10 a) is relatively constant across the whole cloud field

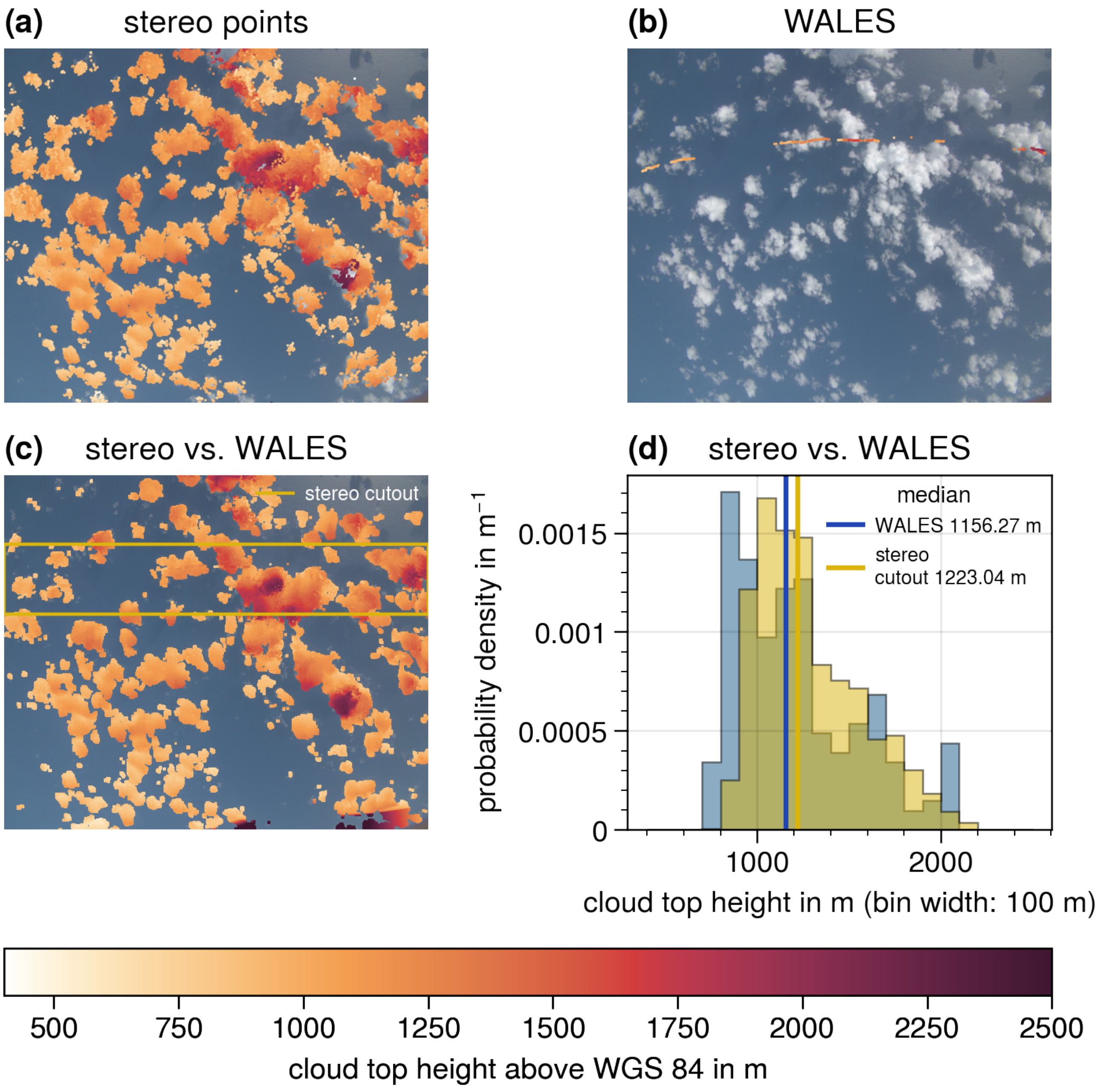

Figure 10. Cloud top height (CTH) data of the case study of small cumulus clouds. The measurement was taken on 2020-02-02 at 18:29:30 UTC. a) CTH of stereo points from the stereographic reconstruction method; b) CTH from the WALES lidar system; c) Interpolated CTH based on the stereo points. The WALES CTH is plotted on top and the yellow rectangle indicates a specMACS cutout surrounding the WALES track. Panel d) shows the probability densities of the CTHs of the specMACS cutout (yellow) and the WALES measurements (blue). The RGB measurement of the cloud field is shown in the background of the panels a), b), and c). The colorbar at the bottom corresponds to all cloud top height measurements shown in the panels a), b) and c).

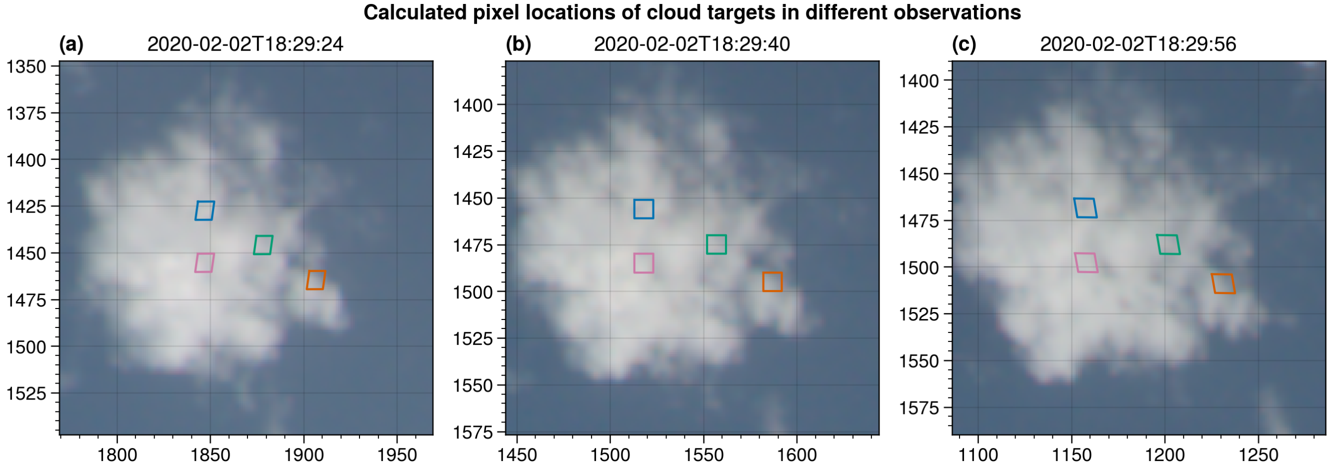

Figure 11. Calculated pixel positions of cloud targets, indicated by different colors, in observations at different times during the overflight.

with a median value of about 1200 m. Some (diameter wise) larger and more developed clouds also have higher cloud tops up to 2200 m. Cloud top height data derived from WALES lidar measurements are projected onto the specMACS RGB image and are shown in Fig. 10 b). The lidar measurements are also plotted on top of the stereo points, which were interpolated onto the whole image (Fig. 10 c). The stereographic result is again very similar to the WALES measurements. This is also evident in panel d), where the probability density of the stereo data in the surroundings of the WALES track (yellow rectangle in Panel c) is plotted along with the WALES cloud top height data (blue).

The stereographic approach determines the cloud height by finding the ideal match between the known viewing directions during the overpass and the connecting line between identified targets at cloud top and the aircraft. Or in other words, the method guarantees the best possible tracking of targets at cloud top, except for a remaining residuum / mispointing error, which is exactly what we require for the cloudbow retrieval. The already discussed imperfect geometric calibration (horizontal offset of up to 100 m) also affects the stereographic detection, and a deviation of the derived cloud top height from the actual cloud top height is expected. Nevertheless, using this potentially biased cloud top height, together with the biased geometric calibration and the wind correction, allows proper tracking of the cloud targets in different images. We manually verified the tracking of cloud targets with distinctive features during the overflight. One such example is shown in Fig. 11. Based on the location of the targets and the ambient wind at 18:29:40 UTC, the pixel positions of the targets in other images are calculated. A visual comparison of the identified targets in the different images shows that the targets are successfully tracked and the offset between the different images is small. Due to camera distortions the shape of the originally rectangular cloud targets (at 18:29:40 UTC) increasingly takes the shape of a trapezoid. In summary, although the three error sources (geometric calibration, cloud top height, and horizontal wind) affect the geolocalization, the cloudbow retrieval is affected to a much lesser degree. Nevertheless, the error introduced by incorrect geolocalization has yet to be estimated quantitatively.

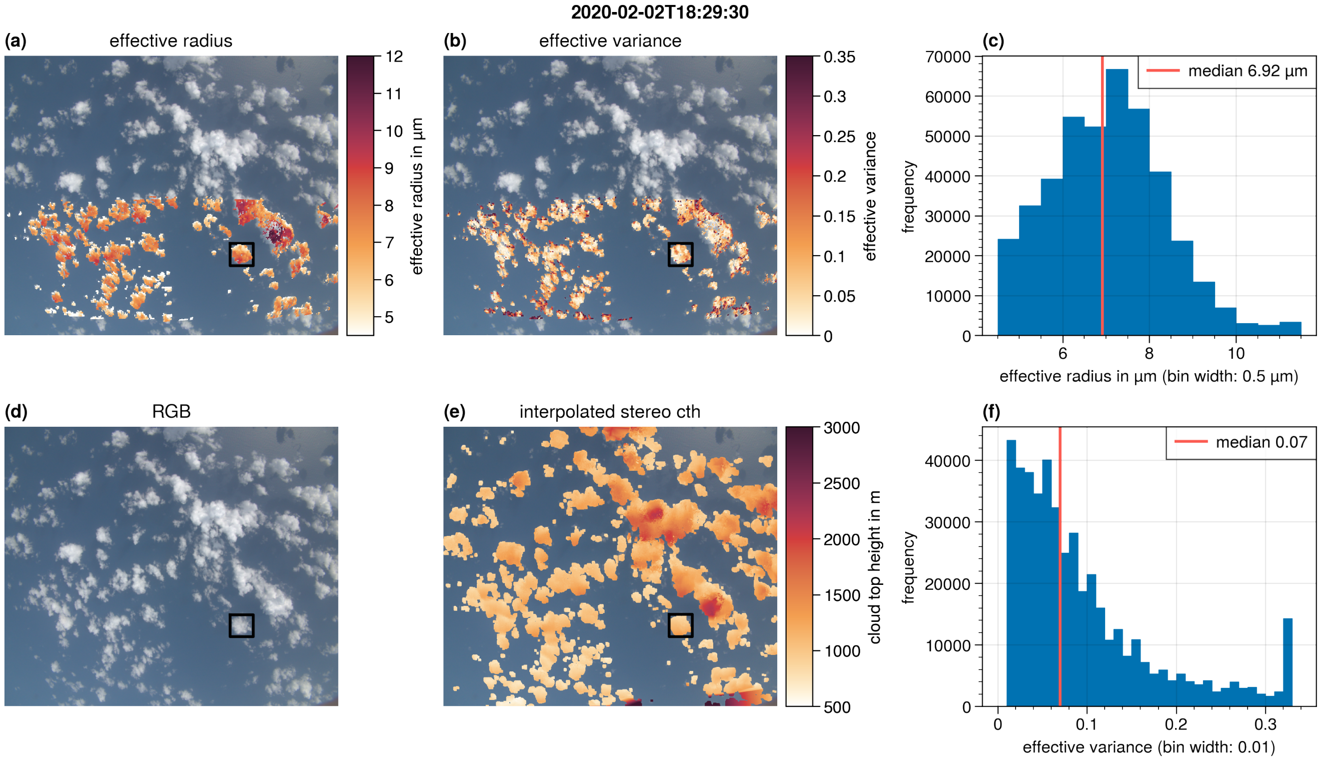

Figure 12. Spatial distribution of effective radius (left) and effective variance (right) for case study 2 presented in Fig. 10. The retrieval is applicable to the area observed within 135° to 165° in scattering angle by aggregating successive images. The black rectangle marks a single cloud, that is presented in Fig. 14.

The retrieved r_{eff} and v_{eff} maps are shown in Fig. 12 a) and b). The frequency distributions of the two parameters are shown in Fig. 12 c) and f). Compared to case study 1, r_{eff} is much smaller (median: $6.92\,\mu\mathrm{m}$) and has a more narrow distribution. Values of r_{eff} larger than $20\,\mu\mathrm{m}$ are not observed. The spatial distribution of r_{eff} is homogeneous and has only few outliers. For higher cloud tops, an increase in r_{eff} is observed. The vertical profile of the effective radius is shown in Fig. 13. The effective radius strongly increases from about $4.5\,\mu\mathrm{m}$ at a cloud top height of $800\,\mathrm{m}$ to $9\,\mu\mathrm{m}$ at $1300\,\mathrm{m}$.

The effective variance (Fig. 12 b and f) is small (median $v_{\mathrm{eff}} = 0.07$) and consistent within the inner part of the clouds. There are some outliers, that occur mainly at the edge of the cloud. This may be due to several reasons: First, especially at the edge of the cloud, a small offset in the geolocation can have a significant impact on the aggregated observations. The offset between the assumed location and the actual location may increase during the aggregation process and could even include ocean measurements for targets at the cloud edge. In this case, the aggregated measurements originate from different targets and the cloudbow signal broadens or vanishes completely. Furthermore, it could also be a physical effect: If entrainment and (inhomogeneous) mixing of dry air occurs in the cloud, modeling studies predict a broadening (increase of v_{eff}) of the droplet

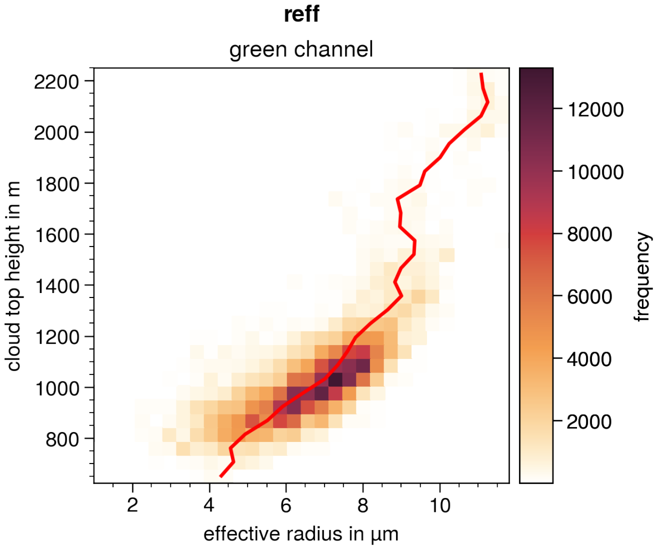

Figure 13. Vertical profile of the retrieved effective radius of the cloud field shown in Fig. 12. The red line indicates the average effective radius for each vertical layer.

size distribution (Pinsky et al., 2016). Such questions will be investigated in the future using the high-resolution specMACS data.

The black rectangle in Fig. 12 marks a single cloud (diameter 1.5 km) that is presented in more detail in Fig. 14. In this figure, maps of the effective radius, the effective variance and the cloud top height are shown together with the frequency distributions of r_{eff} and v_{eff} of the single cloud. The high spatial resolution of the measurements reveals small scale structures of the cloud droplet size distribution, especially regarding the effective variance, that is, e.g., increased within a stream from the top left to the center of the cloud. Three targets of the cloud are selected (marked by circles in the maps). The targets a) and b) have similar r_{eff} but differ in the effective variance. Target c) lies within the region of increased cloud top height, where r_{eff} is also large. The difference of these three targets is visible in the aggregated cloudbow observations presented in Fig. 15, which vary especially regarding the number and visibility of secondary minima. The observations are more noisy compared to the observations of case study 1 (Fig. 9), and also the absolute values of the cloudbow signals are less strong. This indicates, that even within one target the variability of the cloudbow signal is relatively large. A further reduction of the size of a target would be helpful, but this comes with the need of an even increased precision in geolocalization. Although the observations are more noisy, the primary cloudbow is still very pronounced which indicates that the retrieval of r_{eff} is robust. Furthermore, r_{eff} is for all three targets relatively small (6.54 µm to 9.2 µm). In this size range, the cloudbow signal depends strongly on r_{eff} (see Fig. 5). The result of v_{eff} is more difficult: The structure of the supernumerary bows (which mainly defines v_{eff}) can get smoothed out while averaging the signals of different cloud droplet size distributions within the averaging target and the resulting cloud droplet size distribution is in the worst case different from any of the actual sub pixel distributions. A sensitivity analysis of the

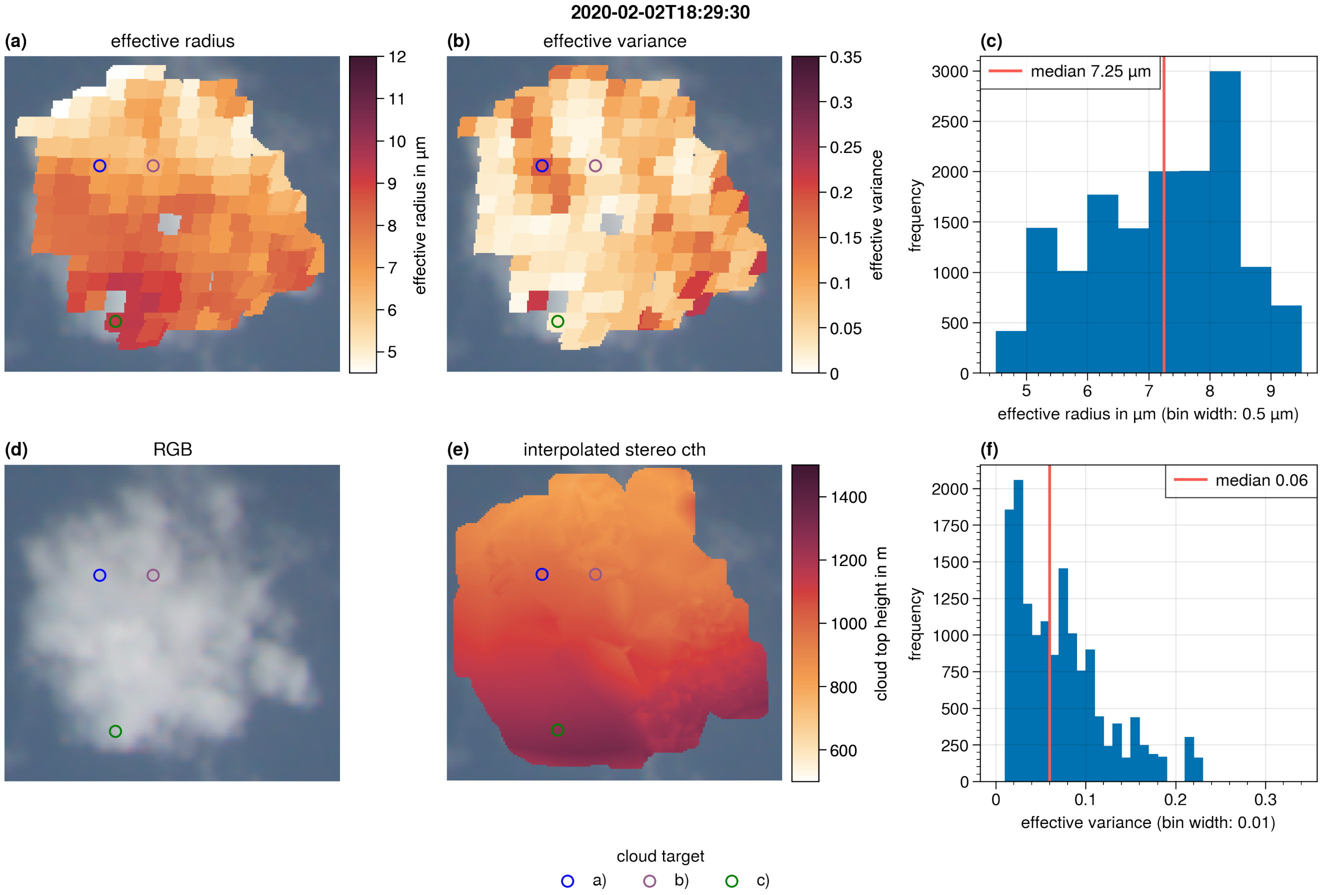

Figure 14. Spatial distribution of effective radius (left) and effective variance (right) for zoom into one cloud shown in case study 2 (Fig. 10 and Fig. 12).

cloudbow algorithm based on different resolutions of airHARP data was presented in McBride et al. (2020) to identify effects of sub pixel variability. This analysis showed that in the case of a wide spread of the cloud droplet size distributions within the sub pixels, the coarse resolution result does not reflect the mean of the sub pixels, as the combination of different gamma size distributions from the subpixels is not another gamma size distribution (Shang et al., 2015). In the future, the specMACS retrieval will be applied to even smaller targets which will further reduce effects of subpixel variability. 460

5 Summary and Outlook

We used the measurements of the new polarization resolving cameras of specMACS to retrieve the effective radius and effective variance of the cloud droplet size distribution at the cloud top. The method relies on polarized measurements of the cloudbow which is sensitive to r_{eff} and v_{eff}. Cloud top height data from an existing stereographic retrieval (Kölling et al., 2019) are

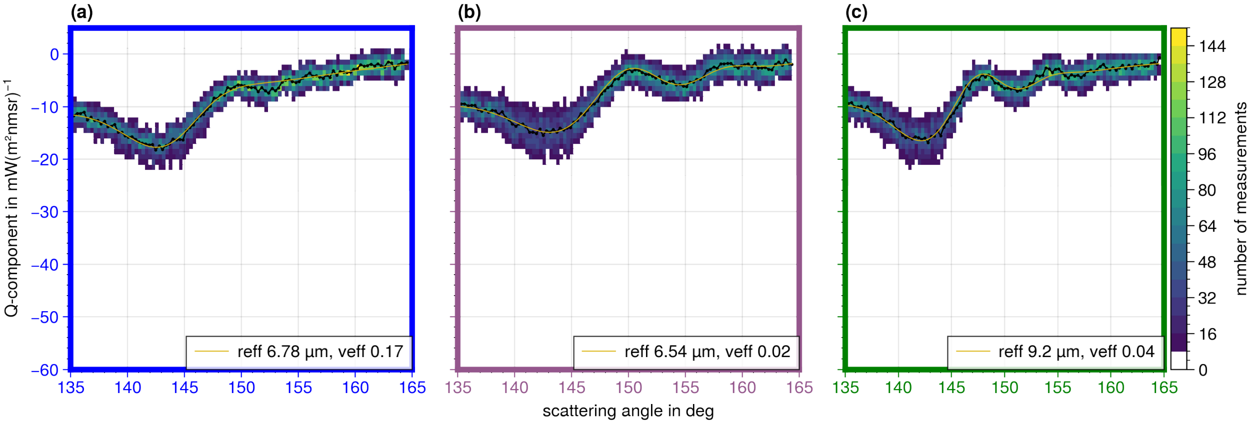

Figure 15. The aggregated polarized radiance measurements of the green channel of the locations shown in Fig. 14 were binned into small boxes with a vertical size of $1\,\mathrm{mW\,m^{-2}\,nm^{-1}\,sr^{-1}}$ and a horizontal size of 0.3°. The number of measurements within a box is indicated by the color of the box. Furthermore, the raw data are binned to 0.3° resolution in scattering angle (black dots connected by black lines). The yellow lines indicate the best fitting simulations. The parameters r_{eff} and v_{eff} of the best fitting simulations are shown in the boxes in the lower right. For better visual comparison with the aggregated measurements of the first case study, the y-axis covers the same range as in Fig. 9.

combined with the measured airplane position and attitude data to geolocate the measurements. A parametric fit is applied to all data points that contain the full cloudbow signature (scattering angle 135° to 165°). The results of the cloudbow retrieval are combined into spatial maps of r_{eff} and v_{eff} that give new insights into cloud microphysics and the spatial distribution of the parameters at the cloud top. The maps reveal structures within the cloud, that are linked to dynamic processes. We presented two case studies of the EUREC^{4}A campaign. The first study shows a stratiform cloud with two (mostly non-overlapping) cloud layers at different heights. In the higher cloud layer very large r_{eff} ($25\,\mu\mathrm{m}$ to $40\,\mu\mathrm{m}$) are retrieved. These values correlate with large radar reflectivity values indicating large droplets and precipitation. The spatial maps are rather smooth and have only few outliers. The high spatial resolution of the retrieval results (currently about $100\,\mathrm{m} \times 100\,\mathrm{m}$) allows the observation of small cumulus clouds, that can be evaluated accurately using the polarimetric cloudbow technique. This is demonstrated in the second case study which shows cumulus clouds with diameters of $1\,\mathrm{km}$ to $2\,\mathrm{km}$. The retrieved effective radii are much smaller ($3\,\mu\mathrm{m}$ to $12\,\mu\mathrm{m}$) and the effective variances increase from the cloud center to the edge with a median value of 0.07 During EUREC^{4}A many similar cloud fields were observed. Further evaluations of such cloud fields will include studying the effect of entrainment and mixing processes on the cloud droplet size distribution of small cumulus clouds in more detail.

We assessed how often the cloudbow retrieval can actually be applied during typical observation conditions. Only measurements that cover the whole scattering angle range 135° to 165° are evaluated (see evaluable stripes in Fig. 7 and Fig. 12). Although we need this special observation geometry, the acquired cloudbow dataset is very large: During daytime with optimal cloudbow conditions due to high solar zenith angle, approximately 45 % of the whole field of view can be analyzed which corresponds to an $8\,\mathrm{km}$ wide swath at $10\,\mathrm{km}$ flight altitude. On average and for each polarization camera, a stripe with 17 %

of all pixels of an image can be evaluated (averaged over all EUREC^{4}A measurements). When combining the measurements of the two cameras, the (geometrically) evaluable stripe covered at least 35 % of the single measurements during more than 70 of the approximately 130 total flight hours of EUREC^{4}A. It should be noted, that several EUREC^{4}A HALO flights were partly conducted during nighttime (Konow et al., 2021), during which the observation of the cloudbow is of course impossible. A recent study by Thompson et al. (2022) evaluated the sampled scattering angle range of multi-angle satellite instruments depending on different factors such as solar and view geometry, or location, season, and swath width in more detail.

A statistical evaluation of all EUREC^{4}A flights, with special attention to the differences in cloud microphysics for the different mesoscale cloud patterns (Sugar, Gravel, Fish, Flower) is planned. Further processing steps will include comparisons of the polarimetric retrieval with bi-spectral retrievals both from specMACS, and from satellites such as MODIS and GOES, and validation of the polarimetric retrieval with in situ measurements. During EUREC^{4}A the British research airplane Twin Otter and the french airplane ATR-42 collected measurements inside the clouds, which will be compared to our results. Further validation is planned with in situ data of the recent CIRRUS-HL (2021) and HALO-(AC)3 (2022) campaigns. In addition, the retrieval will also be applied to the spatially limited, but very precise measurements of the backscatter glory.

specMACS offers great potential for further evaluations of clouds: In future, the measurements of the different specMACS cameras (polarimetric and hyperspectral) will be combined to retrieve information about the variation of cloud microphysical properties with height inside the cloud, and to identify the thermodynamic phase of the observed clouds. Furthermore, the HALO remote sensing payload makes it possible to deepen the understanding of clouds by combining the measurements of the different instruments.

Data availability. The specMACS data used in this study are available upon request from the corresponding author.

Author contributions. TK, TZ, BM and VP actively participated in the EUREC^{4}A field campaign. TK, TZ, BM prepared the field campaign, and provided valuable input during the development of the method. TK designed the data file format, developed the stereo method, and provided software for initial use. LV improved the stereo method, and applied it to the data of the EUREC^{4}A field campaign. AW carried out the geometric calibration of the cameras and provided the software code to process and calibrate the raw data. CE provided valuable input about polarization. BM and CE helped carry out the phase matrix simulations. VP developed the polarimetric cloudbow algorithm, processed and visualized the data and wrote the manuscript with input from all coauthors.

Competing interests. Some authors are members of the editorial board of Atmospheric Measurement Techniques. The peer-review process was guided by an independent editor, and the authors have also no other competing interests to declare.

Acknowledgements. Thank you, Bjorn Stevens, MPI for Meteorology Hamburg and Markus Rapp, Institut für Physik der Atmosphäre, DLR Oberpfaffenhofen for funding the specMACS contribution to EUREC^{4}A. Thanks also go to Linda Forster, who supported us during the EUREC^{4}A measurements. We thank the EUREC^{4}A project team for collaboration and support and special thanks go to the DLR flight operations team for the planning and the execution of the HALO flights. Furthermore, we thank Andreas Giez, Vladyslav Nenakhov and Martin Zöger for valuable information about the BAHAMAS dataset. Thank you, Silke Groß and Martin Wirth for providing the WALES lidar data. Many thanks to Alexander Scheiderer and Zhoutong Ma, for developing the cloud mask algorithm. Thank you, Heike Konow and Lutz Hirsch for sharing the HAMP radar data and for providing valuable information about the data. The data used in this publication was gathered in the EUREC4A field campaign and is made available through Meteorologisches Institut, Ludwig-Maximilians-Universität München. EUREC^{4}A is funded with support of the European Research Council (ERC), the Max Planck Society (MPG), the German Research Foundation (DFG), the German Meteorological Weather Service (DWD) and the German Aerospace Center (DLR).

References

Alexandrov, M. D., Cairns, B., Emde, C., Ackerman, A. S., and van Diedenhoven, B.: Accuracy assessments of cloud droplet size retrievals from polarized reflectance measurements by the research scanning polarimeter, Remote Sens. Environ., 125, 92–111, https://doi.org/10.1016/j.rse.2012.07.012, 2012a.

Alexandrov, M. D., Cairns, B., and Mishchenko, M. I.: Rainbow Fourier transform, Journal of Quantitative Spectroscopy and Radiative Transfer, 113, 2521–2535, https://doi.org/https://doi.org/10.1016/j.jqsrt.2012.03.025, electromagnetic and Light Scattering by non-spherical particles XIII, 2012b.

Alexandrov, M. D., Cairns, B., Wasilewski, A. P., Ackerman, A. S., McGill, M. J., Yorks, J. E., Hlavka, D. L., Platnick, S. E., Thomas Arnold, G., van Diedenhoven, B., Chowdhary, J., Ottaviani, M., and Knobelspiesse, K. D.: Liquid water cloud properties during the Polarimeter Definition Experiment (PODEX), Remote Sensing of Environment, 169, 20–36, https://doi.org/https://doi.org/10.1016/j.rse.2015.07.029, 2015.

Alexandrov, M. D., Cairns, B., van Diedenhoven, B., Ackerman, A. S., Wasilewski, A. P., McGill, M. J., Yorks, J. E., Hlavka, D. L., Platnick, S. E., and Arnold, G. T.: Polarized view of supercooled liquid water clouds, Remote Sens. Environ., 181, 96–110, https://doi.org/10.1016/j.rse.2016.04.002, 2016.

Alexandrov, M. D., Cairns, B., Sinclair, K., Wasilewski, A. P., Ziemba, L., Crosbie, E., Moore, R., Hair, J., Scarino, A. J., Hu, Y., Stamnes, S., Shook, M. A., and Chen, G.: Retrievals of cloud droplet size from the research scanning polarimeter data: Validation using in situ measurements, Remote Sensing of Environment, 210, 76–95, https://doi.org/https://doi.org/10.1016/j.rse.2018.03.005, 2018.

Bass, M., Stryland, E. W. V., Williams, D. R., and Wolfe, W. L.: Handbook of Optics Volume II Devices, Measurements, and Properties 2nd edition., Handbook of Optics Volume II Devices, 1995.

Bony, S. and Dufresne, J.-L.: Marine boundary layer clouds at the heart of tropical cloud feedback uncertainties in climate models, Geophysical Research Letters, 32, https://doi.org/https://doi.org/10.1029/2005GL023851, 2005.

Bony, S., Stevens, B., Ament, F., Bigorre, S., Chazette, P., Crewell, S., Delanoë, J., Emanuel, K., Farrell, D., Flamant, C., Gross, S., Hirsch, L., Karstensen, J., Mayer, B., Nuijens, L., Ruppert, J. H., Sandu, I., Siebesma, P., Speich, S., Szczap, F., Totems, J., Vogel, R., Wendisch, M., and Wirth, M.: EUREC4A: A Field Campaign to Elucidate the Couplings Between Clouds, Convection and Circulation, Surveys in Geophysics, 38, 1529–1568, https://doi.org/10.1007/s10712-017-9428-0, 2017.

Bony, S., Schulz, H., Vial, J., and Stevens, B.: Sugar, Gravel, Fish, and Flowers: Dependence of Mesoscale Patterns of Trade-Wind Clouds on Environmental Conditions, Geophysical Research Letters, 47, e2019GL085 988, https://doi.org/https://doi.org/10.1029/2019GL085988, e2019GL085988 10.1029/2019GL085988, 2020.

Bradski, G.: The OpenCV Library, Dr. Dobb's Journal of Software Tools, 2000.

Brenguier, J.-L. and Chaumat, L.: Droplet Spectra Broadening in Cumulus Clouds. Part I: Broadening in Adiabatic Cores, Journal of the Atmospheric Sciences, 58, 628 – 641, https://doi.org/10.1175/1520-0469(2001)058<0628:DSBICC>2.0.CO;2, 2001.

Bréon, F.-M. and Doutriaux-Boucher, M.: A comparison of cloud droplet radii measured from space, IEEE Transactions on Geoscience and Remote Sensing, 43, 1796–1805, 2005.

Bréon, F.-M. and Goloub, P.: Cloud droplet effective radius from spaceborne polarization measurements, Geophysical research letters, 25, 1879–1882, 1998.

Cairns, B., Russell, E. E., and Travis, L. D.: The Research Scanning Polarimeter: Calibration and ground-based measurements, in: Polarization: Measurement, Analysis, and Remote Sensing II, 18 Jul. 1999, Denver, Col., vol. 3754 of *Proc. SPIE*, p. 186, https://doi.org/10.1117/12.366329, 1999.

Diner, D. J., Xu, F., Garay, M. J., Martonchik, J. V., Rheingans, B. E., Geier, S., Davis, A., Hancock, B., Jovanovic, V., Bull, M., et al.: The Airborne Multiangle SpectroPolarimetric Imager (AirMSPI): a new tool for aerosol and cloud remote sensing, Atmospheric Measurement Techniques, 6, 2007–2025, 2013.

Emde, C., Buras, R., Mayer, B., and Blumthaler, M.: The impact of aerosols on polarized sky radiance: model development, validation, and applications, Atmospheric Chemistry and Physics, 10, 383–396, https://doi.org/10.5194/acp-10-383-2010, 2010.

Emde, C., Barlakas, V., Cornet, C., Evans, F., Korkin, S., Ota, Y., Labonnote, L. C., Lyapustin, A., Macke, A., Mayer, B., and Wendisch, M.: IPRT polarized radiative transfer model intercomparison project – Phase A, Journal of Quantitative Spectroscopy and Radiative Transfer, 164, 8–36, https://doi.org/10.1016/j.jqsrt.2015.05.007, 2015.

Emde, C., Buras-Schnell, R., Kylling, A., Mayer, B., Gasteiger, J., Hamann, U., Kylling, J., Richter, B., Pause, C., Dowling, T., and Bugliaro, L.: The libRadtran software package for radiative transfer calculations (version 2.0.1), Geoscientific Model Development, 9, 1647–1672, https://doi.org/10.5194/gmd-9-1647-2016, 2016.

Ewald, F., Kölling, T., Baumgartner, A., Zinner, T., and Mayer, B.: Design and characterization of specMACS, a multipurpose hyperspectral cloud and sky imager, Atmospheric Measurement Techniques, 9, 2015–2042, https://doi.org/10.5194/amt-9-2015-2016, 2016.

Ewald, F., Zinner, T., Kölling, T., and Mayer, B.: Remote sensing of cloud droplet radius profiles using solar reflectance from cloud sides – Part 1: Retrieval development and characterization, Atmospheric Measurement Techniques, 12, 1183–1206, https://doi.org/10.5194/amt-12-1183-2019, 2019.

Fu, D., Di Girolamo, L., Liang, L., and Zhao, G.: Regional Biases in MODIS Marine Liquid Water Cloud Drop Effective Radius Deduced Through Fusion With MISR, Journal of Geophysical Research: Atmospheres, 124, 13 182–13 196, https://doi.org/https://doi.org/10.1029/2019JD031063, 2019.

Fu, D., Di Girolamo, L., Rauber, R. M., McFarquhar, G. M., Nesbitt, S. W., Loveridge, J., Hong, Y., van Diedenhoven, B., Cairns, B., Alexandrov, M. D., Lawson, P., Woods, S., Tanelli, S., Schmidt, S., Hostetler, C., and Scarino, A. J.: An evaluation of the liquid cloud droplet effective radius derived from MODIS, airborne remote sensing, and in situ measurements from CAMP^{2}Ex, Atmospheric Chemistry and Physics, 22, 8259–8285, https://doi.org/10.5194/acp-22-8259-2022, 2022.

Giez, A., Mallaun, C., Nenakhov, V., and Zöger, M.: Calibration of a Nose Boom Mounted Airflow Sensor on an Atmospheric Research Aircraft by Inflight Maneuvers, DLR-Forschungsbericht. DLR-FB-2021-17, https://elib.dlr.de/145969/, 2021.

Grabowski, W. W. and Wang, L.-P.: Growth of Cloud Droplets in a Turbulent Environment, Annual Review of Fluid Mechanics, 45, 293–324, https://doi.org/10.1146/annurev-fluid-011212-140750, 2013.

Hansen, J. E.: Multiple scattering of polarized light in planetary atmospheres part II. Sunlight reflected by terrestrial water clouds, Journal of Atmospheric Sciences, 28, 1400–1426, 1971.

Hansen, J. E. and Travis, L. D.: Light scattering in planetary atmospheres, Space Sci. Rev., 16, 527–610, https://doi.org/10.1007/BF00168069, 1974.

Hersbach, H., Bell, B., Berrisford, P., Biavati, G., Horányi, A., Muñoz Sabater, J., Nicolas, J., Peubey, C., Radu, R., Rozum, I., Schepers, D., Simmons, A., Soci, C., Dee, D., and Thépaut, J.-N.: ERA5 hourly data on pressure levels from 1959 to present., Copernicus climate change service (c3s) climate data store (cds), https://doi.org/10.24381/cds.bd0915c6, (Accessed on 23-08-2022), 2018.

Hersbach, H., Bell, B., Berrisford, P., Hirahara, S., Horányi, A., Muñoz-Sabater, J., Nicolas, J., Peubey, C., Radu, R., Schepers, D., et al.: The ERA5 global reanalysis, Quarterly Journal of the Royal Meteorological Society, 146, 1999–2049, 2020.

IPCC: Climate Change 2021: The Physical Science Basis. Contribution of Working Group I to the Sixth Assessment Report of the Intergovernmental Panel on Climate Change, Cambridge University Press (In Press), https://doi.org/doi:10.1017/9781009157896, 2021.

Knobelspiesse, K., Tan, Q., Bruegge, C., Cairns, B., Chowdhary, J., van Diedenhoven, B., Diner, D., Ferrare, R., van Harten, G., Jovanovic, V., Ottaviani, M., Redemann, J., Seidel, F., and Sinclair, K.: Intercomparison of airborne multi-angle polarimeter observations from the Polarimeter Definition Experiment, Appl. Opt., 58, 650–669, https://doi.org/10.1364/AO.58.000650, 2019.

Kölling, T., Zinner, T., and Mayer, B.: Aircraft-based stereographic reconstruction of 3-D cloud geometry, Atmospheric Measurement Techniques, 12, 1155–1166, https://doi.org/10.5194/amt-12-1155-2019, 2019.

Konow, H., Ewald, F., George, G., Jacob, M., Klingebiel, M., Kölling, T., Luebke, A. E., Mieslinger, T., Pörtge, V., Radtke, J., Schäfer, M., Schulz, H., Vogel, R., Wirth, M., Bony, S., Crewell, S., Ehrlich, A., Forster, L., Giez, A., Gödde, F., Groß, S., Gutleben, M., Hagen, M., Hirsch, L., Jansen, F., Lang, T., Mayer, B., Mech, M., Prange, M., Schnitt, S., Vial, J., Walbröl, A., Wendisch, M., Wolf, K., Zinner, T., Zöger, M., Ament, F., and Stevens, B.: EUREC^{4}A's HALO, Earth System Science Data Discussions, 2021, 1–26, https://doi.org/10.5194/essd-2021-193, 2021.

Krautstrunk, M. and Giez, A.: The Transition From FALCON to HALO Era Airborne Atmospheric Research, pp. 609–624, Springer Berlin Heidelberg, Berlin, Heidelberg, https://doi.org/10.1007/978-3-642-30183-4_37, 2012.

LUCID Vision Labs Inc.: Phoenix 5.0 MP Polarized Tech Ref (PHX050S1-Q, Color, IMX264MYR), https://thinklucid.com/downloads-hub/#tab-phoenix-tech-man, (Accessed on 23-08-2022), 2022a.

LUCID Vision Labs Inc.: Phoenix 5.0 MP Polarization Model (IMX250MZR/MYR), https://thinklucid.com/de/product/phoenix-5-0-mp-polarized-model/, (Accessed on 23-08-2022), 2022b.

Marshak, A., Platnick, S., Várnai, T., Wen, G., and Cahalan, R. F.: Impact of three-dimensional radiative effects on satellite retrievals of cloud droplet sizes, Journal of Geophysical Research: Atmospheres, 111, https://doi.org/https://doi.org/10.1029/2005JD006686, 2006.

Martins, J. V., Fernandez-Borda, R., McBride, B., Remer, L., and Barbosa, H. M.: The harp hype ran gular imaging polarimeter and the need for small satellite payloads with high science payoff for earth science remote sensing, in: IGARSS 2018-2018 IEEE International Geoscience and Remote Sensing Symposium, pp. 6304–6307, IEEE, 2018.

Mayer, B. and Kylling, A.: Technical note: The libRadtran software package for radiative transfer calculations - description and examples of use, Atmospheric Chemistry and Physics, 5, 1855–1877, https://doi.org/10.5194/acp-5-1855-2005, 2005.

Mayer, B., Schröder, M., Preusker, R., and Schüller, L.: Remote sensing of water cloud droplet size distributions using the backscatter glory: a case study, Atmospheric Chemistry and Physics, 4, 1255–1263, https://doi.org/10.5194/acp-4-1255-2004, 2004.

McBride, B. A., Martins, J. V., Barbosa, H. M., Birmingham, W., and Remer, L. A.: Spatial distribution of cloud droplet size properties from Airborne Hyper-Angular Rainbow Polarimeter (AirHARP) measurements, Atmospheric Measurement Techniques, 13, 1777–1796, 2020.

Mech, M., Orlandi, E., Crewell, S., Ament, F., Hirsch, L., Hagen, M., Peters, G., and Stevens, B.: HAMP – the microwave package on the High Altitude and LOng range research aircraft (HALO), Atmospheric Measurement Techniques, 7, 4539–4553, https://doi.org/10.5194/amt-7-4539-2014, 2014.

Mie, G.: Beiträge zur Optik trüber Medien, speziell kolloidaler Metallösungen, Annalen der Physik, 330, 377–445, https://doi.org/https://doi.org/10.1002/andp.19083300302, 1908.

Miles, N. L., Verlinde, J., and Clothiaux, E. E.: Cloud Droplet Size Distributions in Low-Level Stratiform Clouds, Journal of the Atmospheric Sciences, 57, 295 – 311, https://doi.org/10.1175/1520-0469(2000)057<0295:CDSDIL>2.0.CO;2, 2000.

Nakajima, T. and King, M. D.: Determination of the Optical Thickness and Effective Particle Radius of Clouds from Reflected Solar Radiation Measurements. Part I: Theory, Journal of Atmospheric Sciences, 47, 1878 – 1893, https://doi.org/10.1175/1520-0469(1990)047<1878:DOTOTA>2.0.CO;2, 1990.

Otsu, N.: A Threshold Selection Method from Gray-Level Histograms, IEEE Transactions on Systems, Man, and Cybernetics, 9, 62–66, https://doi.org/10.1109/TSMC.1979.4310076, 1979.

Painemal, D., Spangenberg, D., Smith Jr., W. L., Minnis, P., Cairns, B., Moore, R. H., Crosbie, E., Robinson, C., Thornhill, K. L., Winstead, E. L., and Ziemba, L.: Evaluation of satellite retrievals of liquid clouds from the GOES-13 imager and MODIS over the midlatitude North Atlantic during the NAAMES campaign, Atmospheric Measurement Techniques, 14, 6633–6646, https://doi.org/10.5194/amt-14-6633-2021, 2021.

Pinsky, M., Khain, A., and Korolev, A.: Theoretical analysis of mixing in liquid clouds – Part 3: Inhomogeneous mixing, Atmospheric Chemistry and Physics, 16, 9273–9297, https://doi.org/10.5194/acp-16-9273-2016, 2016.

Platnick, S.: Vertical photon transport in cloud remote sensing problems, Journal of Geophysical Research: Atmospheres, 105, 22 919–22 935, https://doi.org/https://doi.org/10.1029/2000JD900333, 2000.

Platnick, S., King, M., Ackerman, S., Menzel, W., Baum, B., Riedi, J., and Frey, R.: The MODIS cloud products: algorithms and examples from Terra, IEEE Transactions on Geoscience and Remote Sensing, 41, 459–473, https://doi.org/10.1109/TGRS.2002.808301, 2003.

Platnick, S., Meyer, K. G., King, M. D., Wind, G., Amarasinghe, N., Marchant, B., Arnold, G. T., Zhang, Z., Hubanks, P. A., Holz, R. E., Yang, P., Ridgway, W. L., and Riedi, J.: The MODIS Cloud Optical and Microphysical Products: Collection 6 Updates and Examples From Terra and Aqua, IEEE Transactions on Geoscience and Remote Sensing, 55, 502–525, https://doi.org/10.1109/TGRS.2016.2610522, 2017.

Polonik, P., Knote, C., Zinner, T., Ewald, F., Kölling, T., Mayer, B., Andreae, M. O., Jurkat-Witschas, T., Klimach, T., Mahnke, C., Molleker, S., Pöhlker, C., Pöhlker, M. L., Pöschl, U., Rosenfeld, D., Voigt, C., Weigel, R., and Wendisch, M.: The challenge of simulating the sensitivity of the Amazonian cloud microstructure to cloud condensation nuclei number concentrations, Atmospheric Chemistry and Physics, 20, 1591–1605, https://doi.org/10.5194/acp-20-1591-2020, 2020.

Remer, L. A., Knobelspiesse, K., Zhai, P.-W., Xu, F., Kalashnikova, O. V., Chowdhary, J., Hasekamp, O., Dubovik, O., Wu, L., Ahmad, Z., Boss, E., Cairns, B., Coddington, O., Davis, A. B., Dierssen, H. M., Diner, D. J., Franz, B., Frouin, R., Gao, B.-C., Ibrahim, A., Levy, R. C., Martins, J. V., Omar, A. H., and Torres, O.: Retrieving Aerosol Characteristics From the PACE Mission, Part 2: Multi-Angle and Polarimetry, Frontiers in Environmental Science, 7, https://doi.org/10.3389/fenvs.2019.00094, 2019.

Schulz, H., Eastman, R., and Stevens, B.: Characterization and Evolution of Organized Shallow Convection in the Downstream North Atlantic Trades, Journal of Geophysical Research: Atmospheres, 126, e2021JD034 575, https://doi.org/https://doi.org/10.1029/2021JD034575, e2021JD034575 2021JD034575, 2021.

Shang, H., Chen, L., Bréon, F. M., Letu, H., Li, S., Wang, Z., and Su, L.: Impact of cloud horizontal inhomogeneity and directional sampling on the retrieval of cloud droplet size by the POLDER instrument, Atmospheric Measurement Techniques, 8, 4931–4945, https://doi.org/10.5194/amt-8-4931-2015, 2015.

Shang, H., Letu, H., Bréon, F.-M., Riedi, J., Ma, R., Wang, Z., Nakajima, T. Y., Wang, Z., and Chen, L.: An improved algorithm of cloud droplet size distribution from POLDER polarized measurements, Remote Sensing of Environment, 228, 61–74, https://doi.org/https://doi.org/10.1016/j.rse.2019.04.013, 2019.

Sinclair, K., van Diedenhoven, B., Cairns, B., Alexandrov, M., Dzambo, A. M., and L'Ecuyer, T.: Inference of Precipitation in Warm Stratiform Clouds Using Remotely Sensed Observations of the Cloud Top Droplet Size Distribution, Geophysical Research Letters, 48, e2021GL092 547, https://doi.org/https://doi.org/10.1029/2021GL092547, e2021GL092547 2021GL092547, 2021.

Spinhirne, J. D. and Nakajima, T.: Glory of clouds in the near infrared, Appl. Opt., 33, 4652–4662, https://doi.org/10.1364/AO.33.004652, 1994.

Stevens, B., Ament, F., Bony, S., Crewell, S., Ewald, F., Gross, S., Hansen, A., Hirsch, L., Jacob, M., Kölling, T., Konow, H., Mayer, B., Wendisch, M., Wirth, M., Wolf, K., Bakan, S., Bauer-Pfundstein, M., Brueck, M., Delanoë, J., Ehrlich, A., Farrell, D., Forde, M., Gödde, F., Grob, H., Hagen, M., Jäkel, E., Jansen, F., Klepp, C., Klingebiel, M., Mech, M., Peters, G., Rapp, M., Wing, A. A., and Zinner, T.: A High-Altitude Long-Range Aircraft Configured as a Cloud Observatory: The NARVAL Expeditions, Bulletin of the American Meteorological Society, 100, 1061 – 1077, https://doi.org/10.1175/BAMS-D-18-0198.1, 2019.

Stevens, B., Bony, S., Brogniez, H., Hentgen, L., Hohenegger, C., Kiemle, C., L'Ecuyer, T. S., Naumann, A. K., Schulz, H., Siebesma, P. A., Vial, J., Winker, D. M., and Zuidema, P.: Sugar, gravel, fish and flowers: Mesoscale cloud patterns in the trade winds, Quarterly Journal of the Royal Meteorological Society, 146, 141–152, https://doi.org/https://doi.org/10.1002/qj.3662, 2020.

Stevens, B., Bony, S., Farrell, D., Ament, F., Blyth, A., Fairall, C., Karstensen, J., Quinn, P. K., Speich, S., Acquistapace, C., Aemisegger, F., Albright, A. L., Bellenger, H., Bodenschatz, E., Caesar, K.-A., Chewitt-Lucas, R., de Boer, G., Delanoë, J., Denby, L., Ewald, F., Fildier, B., Forde, M., George, G., Gross, S., Hagen, M., Hausold, A., Heywood, K. J., Hirsch, L., Jacob, M., Jansen, F., Kinne, S., Klocke, D., Kölling, T., Konow, H., Lothon, M., Mohr, W., Naumann, A. K., Nuijens, L., Olivier, L., Pincus, R., Pöhlker, M., Reverdin, G., Roberts, G., Schnitt, S., Schulz, H., Siebesma, A. P., Stephan, C. C., Sullivan, P., Touzé-Peiffer, L., Vial, J., Vogel, R., Zuidema, P., Alexander, N., Alves, L., Arixi, S., Asmath, H., Bagheri, G., Baier, K., Bailey, A., Baranowski, D., Baron, A., Barrau, S., Barrett, P. A., Batier, F., Behrendt, A., Bendinger, A., Beucher, F., Bigorre, S., Blades, E., Blossey, P., Bock, O., Böing, S., Bosser, P., Bourras, D., Bouruet-Aubertot, P., Bower, K., Branellec, P., Branger, H., Brennek, M., Brewer, A., Brilouet, P.-E., Brügmann, B., Buehler, S. A., Burke, E., Burton, R., Calmer, R., Canonici, J.-C., Carton, X., Cato Jr., G., Charles, J. A., Chazette, P., Chen, Y., Chilinski, M. T., Choularton, T., Chuang, P., Clarke, S., Coe, H., Cornet, C., Coutris, P., Couvreux, F., Crewell, S., Cronin, T., Cui, Z., Cuypers, Y., Daley, A., Damerell, G. M., Dauhut, T., Deneke, H., Desbios, J.-P., Dörner, S., Donner, S., Douet, V., Drushka, K., Dütsch, M., Ehrlich, A., Emanuel, K., Emmanouilidis, A., Etienne, J.-C., Etienne-Leblanc, S., Faure, G., Feingold, G., Ferrero, L., Fix, A., Flamant, C., Flatau, P. J., Foltz, G. R., Forster, L., Furtuna, I., Gadian, A., Galewsky, J., Gallagher, M., Gallimore, P., Gaston, C., Gentemann, C., Geyskens, N., Giez, A., Gollop, J., Gouirand, I., Gourbeyre, C., de Graaf, D., de Groot, G. E., Grosz, R., Güttler, J., Gutleben, M., Hall, K., Harris, G., Helfer, K. C., Henze, D., Herbert, C., Holanda, B., Ibanez-Landeta, A., Intrieri, J., Iyer, S., Julien, F., Kalesse, H., Kazil, J., Kellman, A., Kidane, A. T., Kirchner, U., Klingebiel, M., Körner, M., Kremper, L. A., Kretzschmar, J., Krüger, O., Kumala, W., Kurz, A., L'Hégaret, P., Labaste, M., Lachlan-Cope, T., Laing, A., Landschützer, P., Lang, T., Lange, D., Lange, I., Laplace, C., Lavik, G., Laxenaire, R., Le Bihan, C., Leandro, M., Lefevre, N., Lena, M., Lenschow, D., Li, Q., Lloyd, G., Los, S., Losi, N., Lovell, O., Luneau, C., Makuch, P., Malinowski, S., Manta, G., Marinou, E., Marsden, N., Masson, S., Maury, N., Mayer, B., Mayers-Als, M., Mazel, C., McGeary, W., McWilliams, J. C., Mech, M., Mehlmann, M., Meroni, A. N., Mieslinger, T., Minikin, A., Minnett, P., Möller, G., Morfa Avalos, Y., Muller, C., Musat, I., Napoli, A., Neuberger, A., Noisel, C., Noone, D., Nordsiek, F., Nowak, J. L., Oswald, L., Parker, D. J., Peck, C., Person, R., Philippi, M., Plueddemann, A., Pöhlker, C., Pörtge, V., Pöschl, U., Pologne, L., Posyniak, M., Prange, M., Quiñones Meléndez, E., Radtke, J., Ramage, K., Reimann, J., Renault, L., Reus, K., Reyes, A., Ribbe, J., Ringel, M., Ritschel, M., Rocha, C. B., Rochetin, N., Röttenbacher, J., Rollo, C., Royer, H., Sadoulet, P., Saffin, L., Sandiford, S., Sandu, I., Schäfer, M., Schemann, V., Schirmacher, I., Schlenczek, O., Schmidt, J., Schröder, M., Schwarzenboeck, A., Sealy, A., Senff, C. J., Serikov, I., Shohan, S., Siddle, E., Smirnov, A., Späth, F., Spooner, B., Stolla, M. K., Szkółka, W., de Szoeke, S. P., Tarot, S., Tetoni, E., Thompson, E., Thomson, J., Tomassini, L., Totems, J., Ubele, A. A., Villiger, L., von Arx, J., Wagner, T., Walther, A., Webber, B., Wendisch, M., Whitehall, S., Wiltshire, A., Wing, A. A., Wirth, M., Wiskandt, J., Wolf, K., Worbes, L., Wright, E., Wulfmeyer, V., Young, S., Zhang, C., Zhang, D., Ziemen, F., Zinner, T., and Zöger, M.: EUREC^{4}A, Earth System Science Data Discussions, 2021, 1–78, https://doi.org/10.5194/essd-2021-18, 2021.

Thompson, S. N., van Diedenhoven, B., Colarco, P. R., Castellanos, P., Lian, E., and Martins, J. V.: Analysis of Scattering Angle Sampling by Multi-Angle Imaging Polarimeters for Different Orbit Geometries, Frontiers in Remote Sensing, 3, https://doi.org/10.3389/frsen.2022.836262, 2022.

Twomey, S.: Pollution and the planetary albedo, Atmospheric Environment (1967), 8, 1251–1256, https://doi.org/https://doi.org/10.1016/0004-6981(74)90004-3, 1974.

Wagner, W. and Pruß, A.: The IAPWS formulation 1995 for the thermodynamic properties of ordinary water substance for general and scientific use, Journal of physical and chemical reference data, 31, 387–535, 2002.

Wendisch, M., Macke, A., Ehrlich, A., Lüpkes, C., Mech, M., Chechin, D., Dethloff, K., Velasco, C. B., Bozem, H., Brückner, M., Clemen, H.-C., Crewell, S., Donth, T., Dupuy, R., Ebell, K., Egerer, U., Engelmann, R., Engler, C., Eppers, O., Gehrmann, M., Gong, X., Gottschalk, M., Gourbeyre, C., Griesche, H., Hartmann, J., Hartmann, M., Heinold, B., Herber, A., Herrmann, H., Heygster, G., Hoor, P., Jafariserajehlou, S., Jäkel, E., Järvinen, E., Jourdan, O., Kästner, U., Kecorius, S., Knudsen, E. M., Köllner, F., Kretzschmar, J., Lelli, L., Leroy, D., Maturilli, M., Mei, L., Mertes, S., Mioche, G., Neuber, R., Nicolaus, M., Nomokonova, T., Notholt, J., Palm, M., van Pinxteren, M., Quaas, J., Richter, P., Ruiz-Donoso, E., Schäfer, M., Schmieder, K., Schnaiter, M., Schneider, J., Schwarzenböck, A., Seifert, P., Shupe, M. D., Siebert, H., Spreen, G., Stapf, J., Stratmann, F., Vogl, T., Welti, A., Wex, H., Wiedensohler, A., Zanatta, M., and Zeppenfeld, S.: The Arctic Cloud Puzzle: Using ACLOUD/PASCAL Multiplatform Observations to Unravel the Role of Clouds and Aerosol Particles in Arctic Amplification, Bulletin of the American Meteorological Society, 100, 841 – 871, https://doi.org/10.1175/BAMS-D-18-0072.1, 2019.

Wirth, M.: Cloud top height derived from airborne measurements with the WALES lidar during the EUREC4A field campaign, https://doi.org/10.25326/216, Aeris, 2021.

Wirth, M., Fix, A., Mahnke, P., Schwarzer, H., Schrandt, F., and Ehret, G.: The airborne multi-wavelength water vapor differential absorption lidar WALES: system design and performance, Applied Physics B, 96, 201, https://doi.org/10.1007/s00340-009-3365-7, 2009.

Wiscombe, W. J.: Improved Mie scattering algorithms, Appl. Opt., 19, 1505–1509, https://doi.org/10.1364/AO.19.001505, 1980.

Zhang, Z.: A flexible new technique for camera calibration, IEEE Transactions on Pattern Analysis and Machine Intelligence, 22, 1330–1334, https://doi.org/10.1109/34.888718, 2000.

Zhang, Z., Ackerman, A. S., Feingold, G., Platnick, S., Pincus, R., and Xue, H.: Effects of cloud horizontal inhomogeneity and drizzle on remote sensing of cloud droplet effective radius: Case studies based on large-eddy simulations, Journal of Geophysical Research: Atmospheres, 117, https://doi.org/https://doi.org/10.1029/2012JD017655, 2012.

Zinner, T., Marshak, A., Lang, S., Martins, J. V., and Mayer, B.: Remote sensing of cloud sides of deep convection: towards a three-dimensional retrieval of cloud particle size profiles, Atmospheric Chemistry and Physics, 8, 4741–4757, https://doi.org/10.5194/acp-8-4741-2008, 2008.

Zinner, T., Wind, G., Platnick, S., and Ackerman, A. S.: Testing remote sensing on artificial observations: impact of drizzle and 3-D cloud structure on effective radius retrievals, Atmospheric Chemistry and Physics, 10, 9535–9549, https://doi.org/10.5194/acp-10-9535-2010, 2010.

Zinner, T., Schwarz, U., Kölling, T., Ewald, F., Jäkel, E., Mayer, B., and Wendisch, M.: Cloud geometry from oxygen-A-band observations through an aircraft side window, Atmospheric Measurement Techniques, 12, 1167–1181, https://doi.org/10.5194/amt-12-1167-2019, 2019.